Chapter 2
Morphology of Different Electrodeposited Pure Metal Powders

V.D. Jović, N.D. Nikolić, U. Lačnjevac, B.M. Jović, and K.I. Popov

1
2
3

4   AU1
5

2.1 Introduction

6

As mentioned in other chapters, metal powders obtained by electrolytic   7
processes are mainly dendrites which can spontaneously fall off or   8
can be removed from the electrode by tapping or other similar   9
techniques [1]. Also, powder particles can have other morphological   10
forms, such as flakes or needles, fibrous or spongy, and needle or   11

V.D. Jović (✉) • U. Lačnjevac • B.M. Jović
Department of Materials Science, Institute for Multidisciplinary Research,
University of Belgrade, Kneza Višeslava 1, 11030 Belgrade,
P.O. Box 33, Serbia
e-mail: vladajovic@imsi.rs; uros.lacnjevac@imsi.rs; bjovic@imsi.rs

N.D. Nikolić
ICTM-Institute of Electrochemistry, University of Belgrade,
Njegoseva 12, P.O.B. 473, 11001 Belgrade, Serbia
e-mail: nnikolic@tmf.bg.ac.rs

K.I. Popov
ICTM-Institute of Electrochemistry, University of Belgrade,
Njegoseva 12, P.O.B. 473, 11001 Belgrade, Serbia

Faculty of Technology and Metallurgy, University of Belgrade,
Karnegijeva 4, P.O.B. 3503, 11001 Belgrade, Serbia
e-mail: kosta@tmf.bg.ac.yu

12 cauliflower-like ones, and the shape of powder particles depends on the
13 electrodeposition conditions and the nature of the metal.

14   Some technologically and academically important metal powders,
15 such as copper, silver, nickel, cobalt, lead, and cadmium, are obtained
16 by electrolysis of aqueous solutions.

17   According to Winand [2], metals can be classified into three
18 groups:

19 (a) Normal metals (Cd, Zn, Sn, Ag (silver nitrate solutions), Pb)   AU2
20   which have low melting points, T_m, and high exchange current
21   densities, j_0
22 (b) Intermediate metals [Au, Cu, Ag (silver ammonia complex)],
23   which have moderate T_m and medium j_0
24 (c) Inert metals (Fe, Ni, Co, Pt, Cr, Mn), which have high T_m and low j_0

25   The aim of this chapter is morphological analysis of some of the
26 powders from these groups. Metal powders obtained by the constant
27 and periodically changing regimes of electrolysis are analyzed in detail.

28 ## 2.2 Silver

29 ### *2.2.1 Effect of Exchange Current Density*
30 ### *on the Morphology of Silver Powder Particles*

31 Electrodeposition of silver from nitrate solutions is characterized by
32 the high exchange current densities, j_0 ($j_0 \gg j_L$, j_L is the limiting
33 diffusion current density) [3, 4] and the typical polarization curve
34 obtained from 0.06 M $AgNO_3$, 1.2 M $NaNO_3$, and 0.05 M HNO_3
35 solution is shown in Fig. 2.1 (denoted by "o"). The plateau of the
36 limiting diffusion current density corresponds to the range of over-
37 potentials between 75 and 175 mV. On the other hand, electrodepo-
38 sition of silver from ammonium solutions is characterized by the
39 relation $j_0 < j_L$ [4, 5], and the polarization curve for silver electrode-
40 position obtained from a solution containing 0.1 M $AgNO_3$, 0.5 M
41 $(NH_4)_2SO_4$, and 0.5 M NH_3 is also shown in Fig. 2.1 (denoted by
42 "□"). The plateau of the limiting diffusion current density was
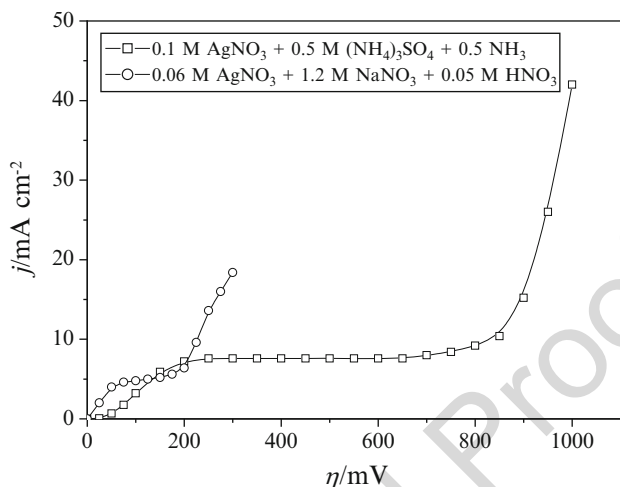
Fig. 2.1 Polarization curves for silver electrodepositions from both 0.1 M AgNO$_3$ + 0.5 M (NH$_4$)$_2$SO$_4$ + 0.5 M NH$_3$ and 0.06 M AgNO$_3$ + 1.2 M NaNO$_3$ + 0.05 M HNO$_3$ (Reprinted from [4] with permission from Electrochemical Society.)

considerably wider, corresponding to the range of overpotentials 43
between 250 and 700 mV. For both the examined solutions, electro- 44
deposition of silver was performed at the room temperature using 45
vertical cylindrical graphite electrodes [4]. The processes of silver 46
electrodeposition from these solutions were not accompanied with 47
hydrogen evolution reaction. 48

Due to the large exchange current density in silver nitrate solutions 49
[3], which is significantly higher than in the case of silver ammonium 50
solution [5], an instantaneous growth of dendrites starts at relatively 51
low overpotential [6]. The silver powder electrodeposited from nitrate 52
electrolyte at an overpotential of 150 mV is shown in Fig. 2.2a. Silver 53
particles obtained by tapping the silver deposit from electrode surface 54
represent a mixture of different morphological forms, as illustrated in 55
Fig. 2.2b–d. Some of the particles had the shape of two-dimensional 56
(2D) dendrites (Fig. 2.2b). The presence of other morphological 57
forms, such as crystals of irregular shape and needle-like particles 58
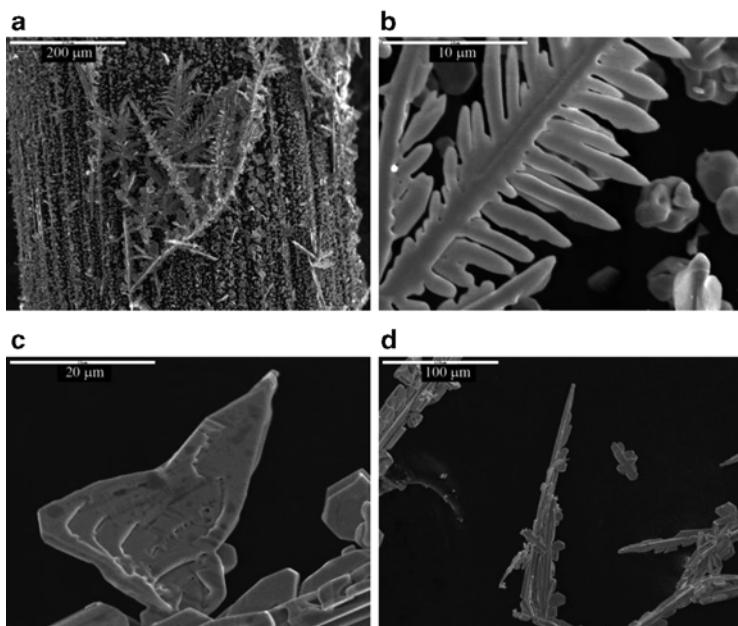(Fig. 2.2c, d), was also noticed. 59

Fig. 2.2 (**a**) Macrostructure and (**b–d**) typical morphological forms of silver obtained by electrodeposition from 0.06 M AgNO$_3$ in both 1.2 M NaNO$_3$ and 0.05 M HNO$_3$ at an overpotential of 150 mV (Reprinted from [4] with permission from Electrochemical Society.)

A typical silver deposit obtained from the ammonium solution at an overpotential of 650 mV is shown in Fig. 2.3a. From Fig. 2.3a, it can be seen that very branchy dendrites are produced at this overpotential. Silver particles obtained by tapping the silver deposit (Fig. 2.3a) are shown in Fig. 2.3b. The dendritic character of this particle is made of the corncob-like elements as presented by the images in Fig. 2.3c, d. A further analysis of the corncob-like elements at the microlevel showed that they are composed of small agglomerates of silver grains (Fig. 2.3d). Anyway, morphologies of silver particles electrodeposited from ammonium solution were completely different than those formed during silver electrodeposition from nitrate electrolyte.
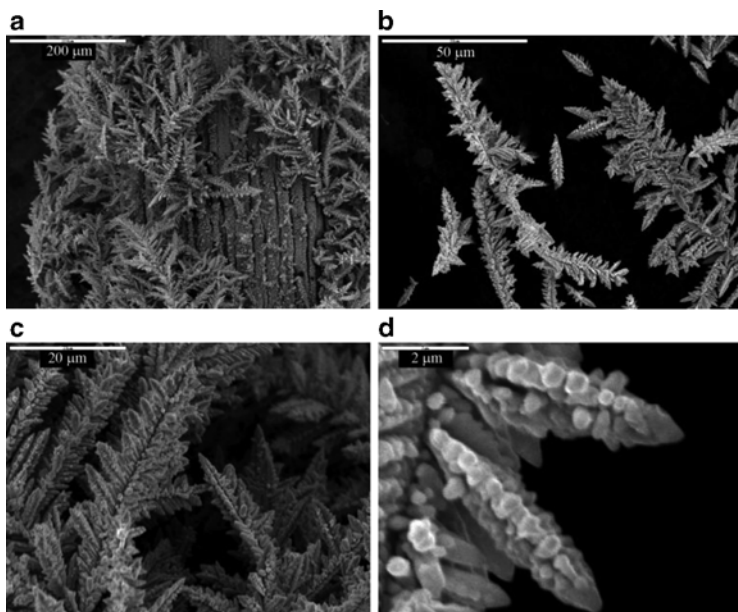
Fig. 2.3 (**a**) Macrostructure of silver powdered deposits electrodeposited at an overpotential of 650 mV from 0.1 M AgNO$_3$ in both 0.5 M (NH$_4$)$_2$SO$_4$ and 0.5 M NH$_3$; (**b**) dendritic particles obtained by tapping this silver deposit; (**c**) and (**d**) the corncob-like elements of which dendrites are composed (Reprinted from [4] with permission from Electrochemical Society.)

It is necessary to note that the shape of the polarization curve for silver electrodeposition from ammonium solution (Fig. 2.1) and morphologies of silver particles (Fig. 2.3) were very similar to those obtained by copper electrodeposition from sulfate solutions at overpotentials corresponding to the plateaus of the limiting diffusion current density [4, 7–11] (see also other chapters). The similarity of silver and copper dendrites was observed at both macro- and micro-levels, because both copper and silver dendrites were composed of corncob-like forms, while the corncob-like forms were built of small agglomerates of metal grains [4].

Also, the sudden increase of the current density with the increasing overpotential above 700 mV is the common characteristic of
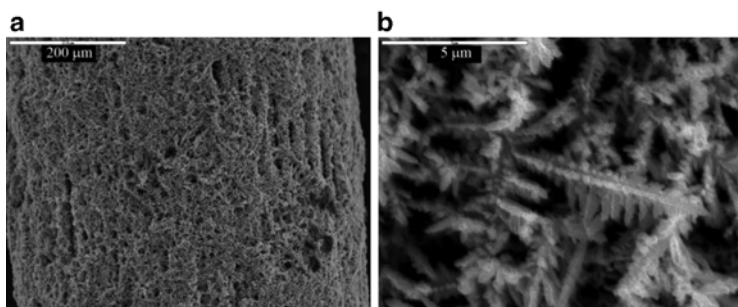
Fig. 2.4 (**a**) Macrostructure of silver powdered deposits electrodeposited at an overpotential of 1,000 mV from 0.1 M $AgNO_3$ in both 0.5 M $(NH_4)_2SO_4$ and 0.5 M NH_3 and (**b**) dendritic particles obtained by tapping silver deposit (Reprinted from [4] with permission from Electrochemical Society.)

both copper electrodeposition from sulfate solution and silver electrodeposition from ammonium solution. Silver powdered deposit obtained from the ammonium solution at an overpotential of 1,000 mV is shown in Fig. 2.4a. At the first sight, spongy-like structure can be noticed from this figure. An analysis of silver deposit produced at the overpotential of 1,000 mV with a higher magnification (Fig. 2.4b) showed that this material is dendritic in shape. Hence, the macrostructure of silver powder formed at an overpotential of 1,000 mV is similar to that of copper and silver deposited at 650 mV. The only difference is in the size of dendrites; silver dendrites electrodeposited at an overpotential of 1,000 mV were considerably smaller than those formed at overpotential of 650 mV, which is attributed to higher nucleation rate at 1,000 mV than at 650 mV [4].

Meanwhile, the macrostructure of the silver deposit produced at an overpotential of 1,000 mV was completely different than that of the copper electrodeposited at the same overpotential. As already mentioned, holes formed by attached hydrogen bubbles surrounded by cauliflower-like agglomerates of copper grains (the honeycomb-like structure; see other chapters) were formed by copper electrodeposition at an overpotential of 1,000 mV [7, 8, 10–13]. The copper powder obtained by tapping the powdered deposit consists of an aggregate of small cauliflower-like particles [14]. Similar copper structures were also observed by electrodeposition at periodically changing rate [15–20].

The observed difference in the morphology of silver and copper deposits produced at an overpotential of 1,000 mV can be ascribed to the simultaneous hydrogen evolution reaction during copper electrodeposition at high overpotentials. In the case of copper, hydrogen evolution commences at some overpotential belonging to the plateau of the limiting diffusion current density, and the increasing overpotential intensifies this reaction [7, 11]. At some overpotential outside the plateau of the limiting diffusion current density, hydrogen evolution becomes vigorous enough to cause a strong stirring of the solution leading to a change of the hydrodynamic conditions in the near-electrode layer. Copper dendrites were formed without and with the quantity of evolved hydrogen which was insufficient to lead to the change of hydrodynamic conditions in the near-electrode layer, while cauliflower-like particles (formed around holes) were obtained with the quantity of evolved hydrogen which was enough to lead to the change of the hydrodynamic conditions in the near-electrode layer [7, 11]. The growth of the current with the increasing overpotential was just a result of parallel hydrogen evolution reaction to copper electrodeposition.

In the case of silver, there is no hydrogen evolution, and the increase in the current with the rising overpotential above 700 mV can be ascribed to the instantaneous dendrite growth. The absence of hydrogen evolution during silver electrodeposition is explained by the fact that the equilibrium potential of silver electrode in silver ammonium solution is slightly more positive than the one of copper electrode in copper sulfate solution [21]. On the other hand, it is well known that the hydrogen evolution reaction on copper electrode is somewhat faster than on silver electrode [22]. Consequently, hydrogen evolution does not occur on silver electrode even at an overpotential of 1,000 mV vs. Ag reference electrode.

2.2.2 Effect of Regime of Pulsating Overpotential on the Shape of Silver Powder Particles

Typical deposits obtained in electrodeposition by constant overpotential are shown in Fig. 2.5. Disperse or irregular deposits
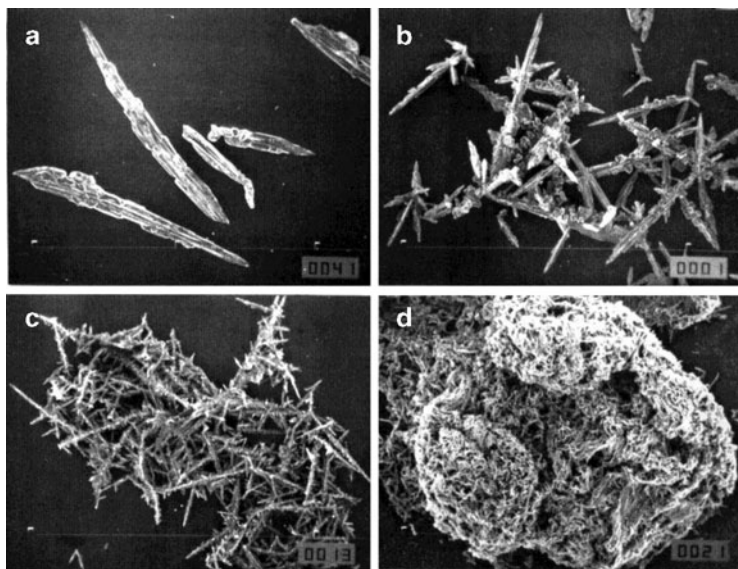
Fig. 2.5 Disperse electrodeposits of silver obtained in constant overpotential deposition at different overpotentials: (**a**) 50 mV, magnification: ×50; (**b**) 100 mV; (**c**) 150 mV; and (**d**) 200 mV; Magnification: ×100 (Reprinted from [23] with permission from the Serbian Chemical Society.)

were obtained at all overpotentials used. In this section, all presented morphologies of silver particles were obtained by electrodepositions from solution containing 0.06 M $AgNO_3$ and 1.2 M $NaNO_3$ in 0.05 M HNO_3 at the room temperature using platinum as the working electrode [23].

Single, nonbranched dendrites were obtained at 50 mV (Fig. 2.5a). Dendrites obtained at 100 mV were occasionally branched (Fig. 2.5b), and some interweaving of the growing dendrites started producing spongy-like agglomerates at 150 mV (Fig. 2.5c). The spongy-like agglomerates obtained at an overpotential of 200 mV were also dendritic, but dendrites are more than ten times shorter than those obtained at lower overpotentials (Fig. 2.6).

The shape of powder particles strongly depends on the type of working electrode used [23]. Agglomeration of silver powder
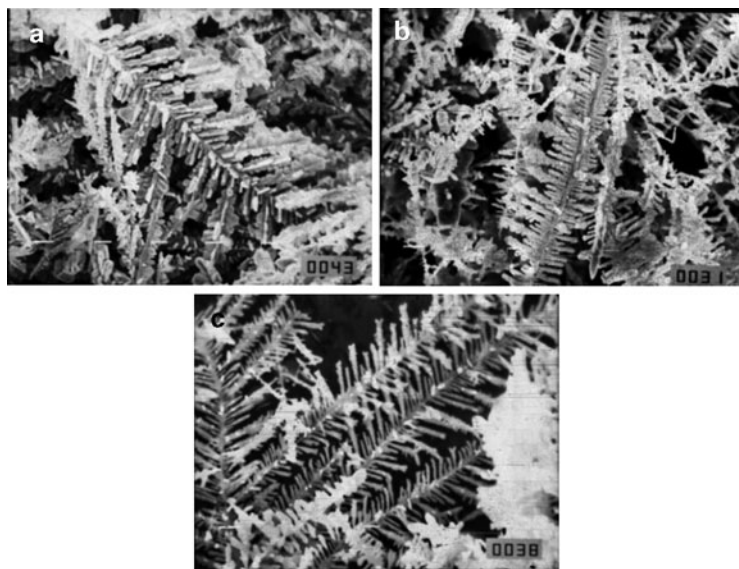
Fig. 2.6 Same as in Fig. 2.5 but (**a**) 200 mV, ×2000; (**b**) 250 mV, ×3500; and (**c**) 300 mV, ×5000 (Reprinted from [23] with permission from the Serbian Chemical Society and copied by permission from the "Electrochemistry Encyclopedia" (http://electrochem.cwru.edu/ed/encycl/) on 04/25/2007. The original material is subject to periodical changes and updates.)

particles was not observed when electrodeposition of silver was performed from the same solution in the overpotential range between 140 and 200 mV onto graphite electrodes [24].

The elimination of agglomerates of powder particles obtained at high overpotentials and the formation of single particles can be realized by treating the powder in an ultrasonic bath [23]. Figure 2.7a shows the single particles obtained by destroying the agglomerates obtained at an overpotential of 200 mV (Fig. 2.5d) in an ultrasonic bath. The detail from Fig. 2.7a is shown in Fig. 2.7b. A similar situation was observed with powder agglomerates formed at over-potentials of 250 and 300 mV [23].

The prevention of formation of agglomerates of particles and the formation of individual particles can be realized by the application of periodically changing regimes of electrolysis [23]. This can be
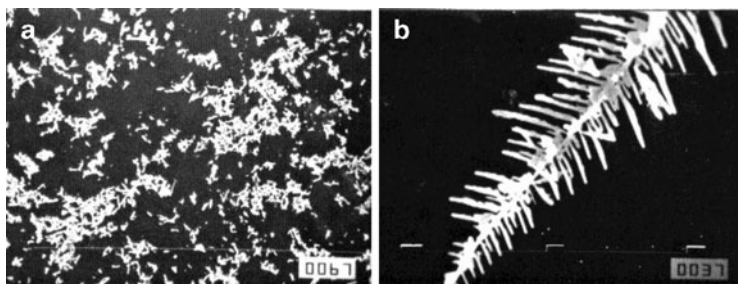
Fig. 2.7 (**a**) Same as in Fig. 2.5d but after treatment in ultrasonic bath: ×100 and (**b**) detail from Fig. 2.7a; ×5000 (Reprinted from [23] with permission from the Serbian Chemical Society.)

explained by the fact that the reversible potential of a surface with a radius of curvature r would depart from that of a planar surface by the quantity [25]:

$$\Delta E = \frac{2\sigma V}{Fr},\tag{2.1}$$

where σ is the interfacial energy between the metal and solution, F is the Faraday constant, V is the molar volume, and r is the protrusion tip radius. For example, this makes the equilibrium potential of spongy zinc deposits 7–10 mV more cathodic than that of zinc foil [26–28]. Obviously, the tips of dendrites characterized by small tip radii will dissolve faster than the flat surface in electrodeposition by all current or overpotential waveforms that are characterized by some anodic current flow [26–30]. In this way, the branching of dendrites is decreased and powder particles become less dendritic and more compact.

Typical deposits obtained by square-wave pulsating overpotential (PO) are shown in Figs. 2.8–2.10. It can be noticed by the analysis of these figures the decrease of both agglomeration and dendritic character of powder particles with the increasing "off" period and decreasing overpotential amplitude.

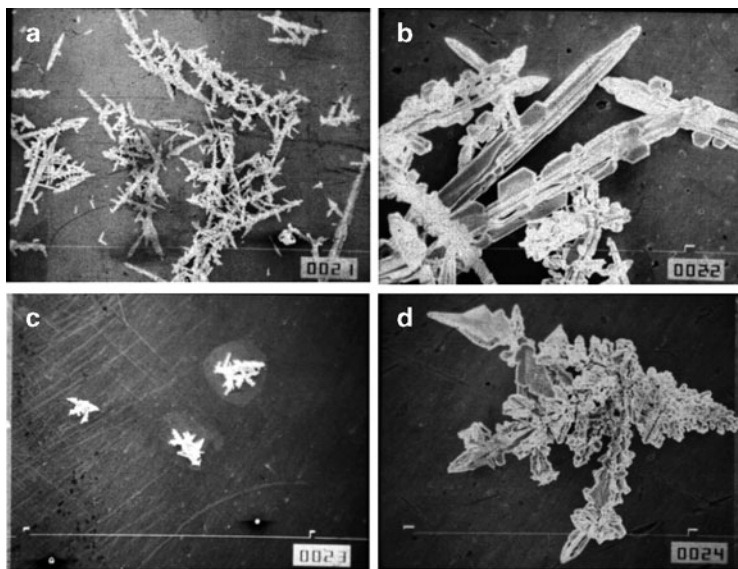This effect was quantitatively discussed for the regime of the square-wave pulsating overpotential [23, 31].

Fig. 2.8 Silver powder particles obtained by square-wave pulsating overpotential. Overpotential amplitude: 300 mV. Pulse duration: 5 ms. (**a**) Pause to pulse ratio: 1, ×100; (**b**) pause to pulse ratio: 1, ×1000; (**c**) pause to pulse ratio: 3, ×100; and (**d**) pause to pulse ratio: 3, ×1000 (Reprinted from [23] with permission from the Serbian Chemical Society.)

Square-wave pulsating overpotential is described by [23, 32]   190

$$\frac{\partial C}{\partial t} = D \frac{\partial^2 C}{\partial x^2}, \tag{2.2}$$

$$C(x,0) = C_0, \tag{2.3}$$

$$C(\delta,t) = C_0, \tag{2.4}$$

$$\frac{\partial C(0,t)}{\partial x} = \frac{j_0}{nFD} \left[\frac{C(0,t)}{C_0} \exp\left(\frac{2.3\eta}{b_c}\right) - \exp\left(-\frac{2.3\eta}{b_a}\right) \right], \tag{2.5}$$
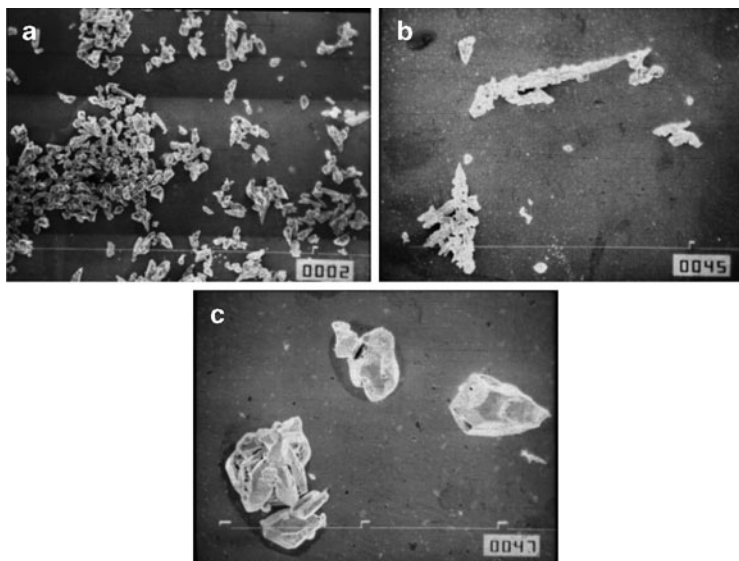
Fig. 2.9 Same as in Fig. 2.8. Overpotential amplitude: 100 mV. Pulse duration: 0.5 s. Pause to pulse ratio: 1: (**a**) ×100, (**b**) ×100; and (**c**) ×500 (Reprinted from [23] with permission from the Serbian Chemical Society.)

191 where j_0 is the exchange current density, n is the number of trans-
192 ferred electrons, D is the diffusion coefficient, b_c and b_a are the
193 cathodic and anodic Tafel slopes, η is the overpotential, C is
194 the concentration, C_0 is the bulk concentration, t is the time, and x
195 is the coordinate in horizontal direction. η is given by

$$\eta = \begin{cases} \eta_A & \text{for} \quad mT_p < t \leq \left(m + \dfrac{1}{p+1}\right)T_p \\[3mm] 0 & \text{for} \quad \left(m + \dfrac{1}{p+1}\right)T_p < t \leq (m+1)T_p \end{cases} \tag{2.6}$$

$$m = 0, 1, 2, \ldots,$$

196 where η_A is the overpotential amplitude, T_p is the period of pulsation,
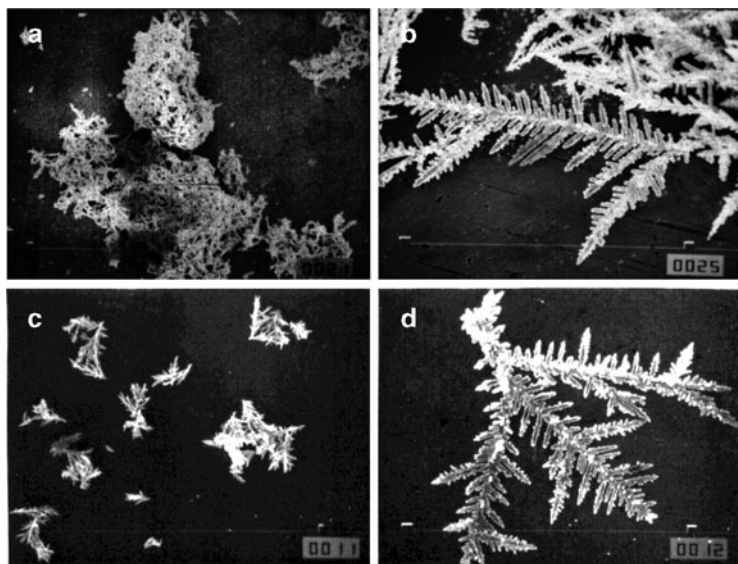197 and p is the pause to pulse ratio.

Fig. 2.10 Same as in Fig. 2.8. Overpotential amplitude: 250 mV. Pulse duration: 0.5 s. (**a**) Pause to pulse ratio: 1, ×100; (**b**) pause to pulse ratio: 1, ×1000; (**c**) pause to pulse ratio: 2, ×100; and (**d**) pause to pulse ratio: 2, ×1000 (Reprinted from [23] with permission from the Serbian Chemical Society.)

Assuming that the surface concentration in pulsating overpotential deposition does not vary with time, at sufficiently high frequencies it is easy to show the response of the current density, j, to the input overpotential:

$$j = \begin{cases} j_0\left(1 - \frac{j_{av}}{j_L}\right)\exp\left(\frac{2.3\eta_A}{b_c}\right) - j_0\exp\left(-\frac{2.3\eta_A}{b_a}\right) \\ \qquad\qquad \text{for} \quad mT_p < t \le \left(m + \frac{1}{p+1}\right)T_p \text{ (a)} \\ -j_{av}\frac{j_0}{j_L} \quad \text{for} \quad \left(m + \frac{1}{p+1}\right)T_p < t \le (m+1)T_p \text{ (b)} \end{cases} \qquad (2.7)$$

where j_{av} is the average current density and j_L is the limiting diffusion current density.

Equations (2.2)–(2.7) are valid for the flat electrode surfaces or protrusions with sufficiently large tip radii where the surface energy

206 term [25] can be neglected. If it cannot be neglected, then the surface
207 energy term affects the reaction rate [33], and for one electron
208 transfer process, it is valid Eq. (2.8):

$$\frac{\partial C}{\partial x} = \frac{j_0}{nFD} \left[\left(1 - \frac{j_{av}}{j_L} \right) \exp\left(-\frac{2\beta\sigma V}{RTr} \right) \exp\left(\frac{2.3\eta}{b_c} \right) \right.$$

$$\left. - \exp\left(\frac{2(1-\beta)\sigma V}{RTr} \right) \exp\left(-\frac{2.3\eta}{b_a} \right) \right], \qquad (2.8)$$

209 where β is a symmetry factor, T is the temperature and R is the gas
210 constant.

211 　　The right-hand side of Eq. (2.5) should be transformed by taking
212 Eq. (2.8) into account. The output current during pauses ($\eta = 0$)
213 becomes

$$j = -j_0 \exp\left(\frac{2(1-\beta)\sigma V}{RTr} \right), \qquad (2.9)$$

214 if $r \rightarrow 0$.

215 　　It is easy to show that the difference between the current density
216 on the flat surface and at the tip of the dendrites during the "off"
217 period:

$$\Delta j = j_0 - j_0 \exp\left(\frac{2(1-\beta)\sigma V}{RTr} \right), \qquad (2.10)$$

218 if $j_{av} \approx j_L$, which leads to

$$h = h_0 + \frac{V j_0}{F} \left[1 - \exp\left(\frac{2(1-\beta)\sigma V}{RTr} \right) \right] t \qquad (2.11)$$

219 because of

$$\frac{dh}{dt} = \frac{V\Delta j}{F}, \qquad (2.12)$$

where h is the height of protrusion and h_0 is the initial height of protrusion, and taking Eq. (2.10) into account,

$$\frac{\mathrm{d}h}{\mathrm{d}t} = \frac{V j_0}{F}\left[1 - \exp\left(\frac{2(1-\beta)\sigma V}{RTr}\right)\right]. \tag{2.13}$$

Equation (2.11) represents the change of the height of the protrusion with tip radius r relative to the flat surface or the protrusion with sufficiently large r. In square-wave PO electrodeposition [29, 34], the filaments on the growing grains formed in spongy electrodeposition can be completely dissolved during the pause leading to the formation of compact deposit. In powder electrodeposition by the same regime, the dissolution of branches on the dendrite stalk is also expected.

Hence, the larger the "off" period, the less dendritic particles are obtained. On the other hand, the current density during the "on" period on the tip of dendrites growing inside the diffusion layer is given by:

$$j = j_0 \frac{h}{\delta} \exp\left(\frac{2.3\eta_{\mathrm{A}}}{b_{\mathrm{c}}}\right), \tag{2.14}$$

which is a somewhat modified Eq. (2.7) [35], where δ is the thickness of diffusion layer. For the same "on" period the particles will be more dendritic with increasing overpotential amplitude. In the millisecond range the ratio between the overpotential corresponding to bulk diffusion control and the activation overpotential can be reduced to the value corresponding to electrodeposition at lower overpotentials in the constant overpotential regime. Hence, deposits obtained in the PO regimes (at the same η_{A} and with different p used) are more similar to those obtained in the constant overpotential regime ($p = 0$) at lower overpotentials than the one corresponding to η_{A} in the PO regimes. The degree of diffusion control decreases with increasing p, even at the limiting diffusion current density, and it can become sufficient to produce the quality of deposits corresponding to mixed, activation, or surface energy control. This will be discussed in more detail in the case of lead electrodeposition.

249   The above discussion well explains the morphologies of silver
250 deposits obtained in the millisecond range (Fig. 2.8), as well as to
251 some extent in the second range (Figs. 2.9 and 2.10). In the latter
252 case, the anodic current decreases during the "off" period, and this
253 effect is also observed in electrodeposition by the regime of pulsating
254 current (PC). In these cases, the dissolution of disperse metal occurs
255 by the mechanism of galvanic microcells at the higher pause to pulse
256 ratios [36–39]. Obviously, the agglomerate formation cannot be
257 completely prevented in this way except at very low overpotential
258 amplitude.

259   The second effect of the application of periodically changing
260 regimes of electrolysis on the morphology of powder particles is that
261 the metal adatoms on the surface, which are not in stable positions,
262 dissolve easier than the atoms from the crystal lattice, permitting the
263 formation of ideal crystal planes on powder particles. Powder particles
264 of silver obtained by pulsating and polarity-reversing techniques are
265 almost small monocrystals [1, 24].

2.3   Lead

267 Electrodeposition of lead belongs to the fast electrochemical
268 processes because it is characterized by a large exchange current
269 density, j_0 [40]. Figure 2.11 shows the polarization curve for lead
270 electrodeposition from solution containing 0.50 M $Pb(NO_3)_2$ in
271 2.0 M $NaNO_3$. All experiments presented here were performed at
272 the room temperature using cylindrical copper wires as the working
273 electrodes [41]. The reference and counter electrodes were of a pure
274 lead. The polarization curve obtained from this solution consisted of
275 two parts. The characteristic of the first part is linear dependence
276 of the current density on the overpotential. After an overpotential of
277 about 100 mV, the current density increased quickly, and this rapid
278 increase of the current with the overpotential is the characteristic of
279 the second part of the polarization curve.

280   The linear dependence of the current density on overpotential
281 corresponds to ohmic-controlled electrodeposition [42, 43]. The mech-
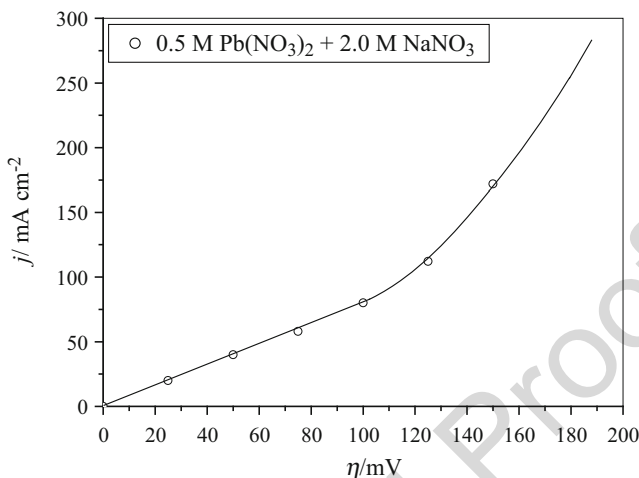282 anism of the ohmic-controlled electrodeposition of metals is presented

Fig. 2.11 Polarization curve for lead electrodeposition from 0.50 M Pb(NO$_3$)$_2$ in 2.0 M NaNO$_3$

in Chap. 1. As already mentioned, for sufficiently fast electrode processes ($j_0/j_L \geq 100$), there is no activation or diffusion polarization before the limiting diffusion current density is reached. At current densities lower than the limiting diffusion ones, the measured overpotential is due to the ohmic voltage drop between the electrode and the tip of Lugin capillary [44]. When the limiting diffusion current density is reached, the process of electrochemical deposition is under complete diffusion control. Meanwhile, as seen from Fig. 2.11, instead of the plateau of the limiting current density the inflection point on the polarization curve was observed. This inflection point on the polarization curve corresponds to an overpotential of about 100 mV. The survey of lead surface morphologies obtained at different overpotentials was the most suitable way to analyze this polarization curve and hence the lead electrodeposition system.

Figures 2.12–2.14 show morphologies of lead deposits obtained in the ohmic-controlled deposition (Fig. 2.12), in the transitional zone corresponding to the end of the ohmic-controlled electrodeposition (Fig. 2.13) and to the zone of rapid increase of the current of electrodeposition (Fig. 2.14).
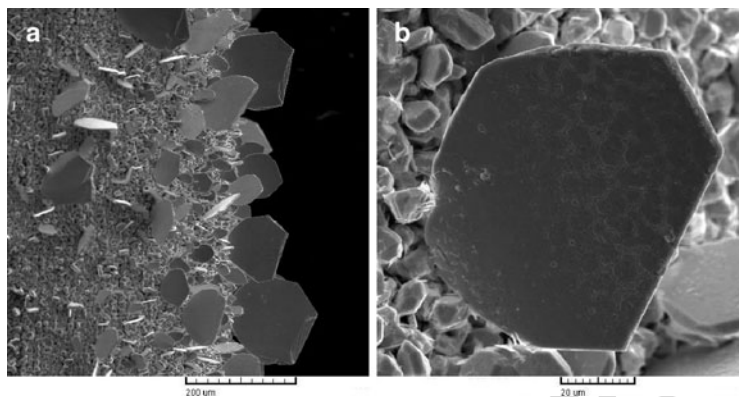
Fig. 2.12 Lead deposits obtained at an overpotential of 50 mV. Time of electrolysis: 180 s
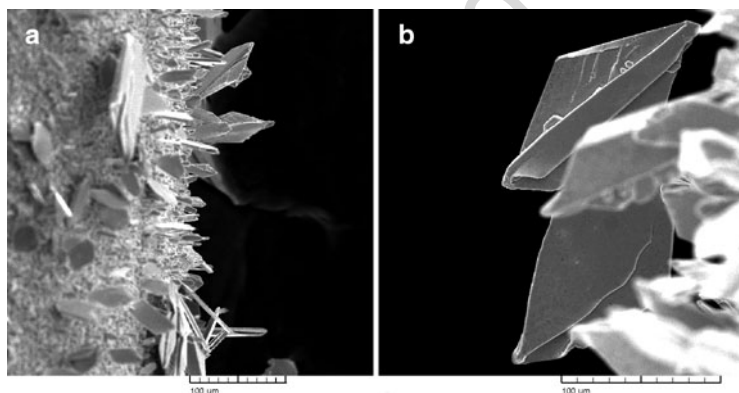

Fig. 2.13 Lead deposits obtained at an overpotential of 100 mV. Time of electrolysis: 60 s

302   The single lead crystals were obtained in ohmic-controlled
303 electrodeposition at an overpotential of 50 mV (Fig. 2.12). The forma-
304 tion of these single crystals was accompanied by a slight increase in the
305 current during the electrodeposition process. Figure 2.13 shows that
306 the mixture of different regular geometric forms from single crystals to
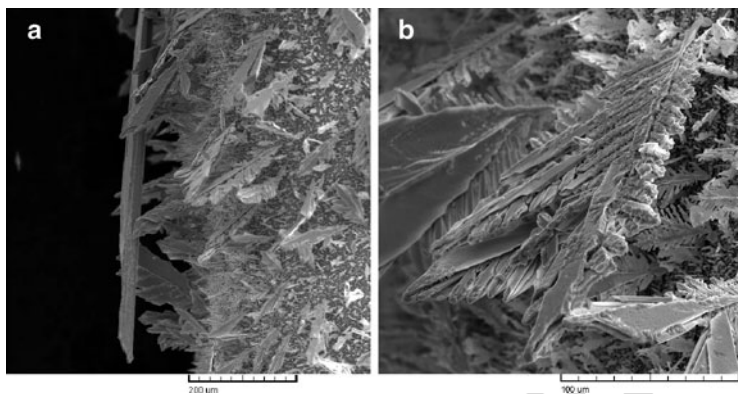307 those given in Fig. 2.13b was obtained at an overpotential of 100 mV

Fig. 2.14 Lead deposits obtained at an overpotential of 150 mV. Time of electrolysis: 20 s

corresponding to the inflection point. The formation of these 308
morphological forms was accompanied by an increase in the current 309
of electrodeposition of about 50% in relation to the initial current of 310
electrodeposition. Finally, the increase of the current during electrode- 311
position processes at overpotentials higher than 100 mV was very quick 312
and the morphology of electrodeposited lead obtained at an 313
overpotential of 150 mV after double increase of current in relation to 314
the initial electrodeposition current is shown in Fig. 2.14. From 315
Fig. 2.14, it can be clearly seen that the single and two-dimensional 316
(2D) lead dendrites were dominant morphological forms obtained at 317
this overpotential (Fig. 2.14). 318

To better clarify the formed morphological forms (especially 319
those obtained at an overpotential of 100 mV), these lead deposits 320
were compared with those obtained in the galvanostatic regime. 321
In the galvanostatic regime, lead electrodeposition was performed 322
at current densities of 100 and 160 mA/cm^2. These current densities 323
corresponded to the final currents during electrodeposition in the 324
potentiostatic regime of electrolysis at overpotentials of 100 and 325
150 mV, respectively. Figures 2.15 and 2.16 show lead deposits 326
obtained at current densities of 100 mA/cm^2 (Fig. 2.15) and 327
160 mA/cm^2 (Fig. 2.16). The single and 2D (two-dimensional) 328
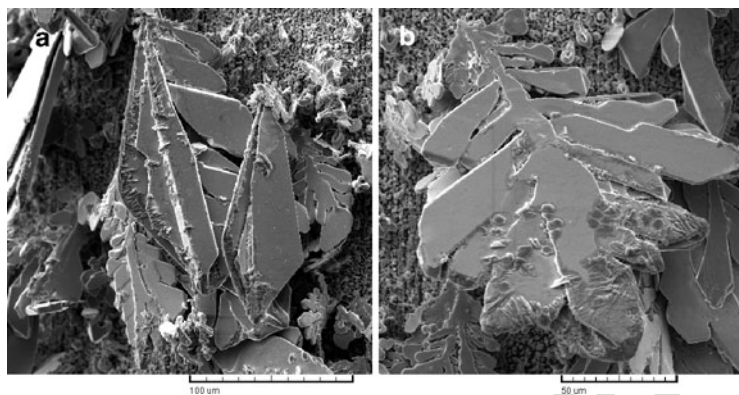dendrites were the dominant morphological forms obtained at the 329

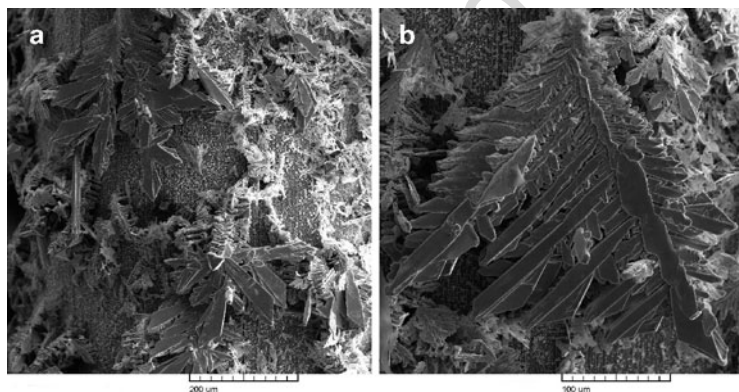**Fig. 2.15** Lead deposits obtained at a current density of 100 mA/cm^2. Time of electrolysis: 60 s

Fig. 2.16 Lead deposits obtained at a current density of 160 mA/cm^2. Time of electrolysis: 20 s

330 both current densities. The shape of 2D dendrites obtained at a current
331 density of 100 mA/cm^2 clearly indicates that the regular geometric
332 forms obtained at an overpotential of 100 mV (Fig. 2.13b) represents
333 the precursors of dendrites.
334   It is necessary to note that dendrites obtained in the galvanostatic
335 regime were more branchy structures than those obtained in the

potentiostatic regime. One of the reasons for it is the fact that during 336
electrodeposition in the galvanostatic regime at the current density of 337
160 mA/cm^2, the initial overpotential was about 220 mV, and the 338
overpotential of about 110 mV was attained after electrodeposition 339
with an electrolysis time of 20 s. A similar situation was also 340
observed during lead electrodeposition at 100 mA/cm^2. 341

The shape of lead dendrites falls under the classical Wranglen's 342
definition of a dendrite. According to Wranglen [45], dendrites con- 343
sist of stalk and primary and secondary branches. From Figs. 2.14–2.16, 344
these elements of dendrites are clearly visible. From the electrochemi- 345
cal point of view, a dendrite is defined as an electrode surface protrusion 346
that grows under activation control, while electrodeposition to the 347
macroelectrode is predominantly under diffusion control [6, 33, 46, 348
47]. For very fast electrodeposition processes, the critical overpotential 349
for dendritic growth initiation, η_I, and the critical overpotential for 350
instantaneous dendritic growth, η_c, depend on the metal surface energy 351
and they are of the order of a few millivolts [6]. The initiation of the 352
dendritic growth is followed by the strong increase of the apparent 353
current density because the current density on the tips of formed 354
dendrites is under mixed activation–diffusion or complete activation 355
control. Hence, the strong increase of current with overpotentials higher 356
than 100 mV corresponds to the activation-controlled electrodeposition 357
on the tips of formed dendrites. On the other hand, the inflection 358
point estimated to be at an overpotential of 100 mV corresponds to 359
the transition between ohmic and activation-controlled electrodeposi- 360
tion process. 361

The two-dimensional forms were only obtained during lead elec- 362
trodeposition. The two-dimensional nucleation was also a character- 363
istic of silver electrodeposition from nitrate solution (Fig. 2.2) [4]. 364
The polarization curve with an inflection point was also obtained in 365
the case of silver electrodeposition from nitrate solution when the 366
strong increase of current density was accompanied by the formation 367
of dendrites [42, 43]. The common characteristic of these metal 368
electrodeposition processes is affiliation to the same group of metals, 369
i.e., to group of normal metals [Cd, Zn, Pb, Sn, Ag (silver nitrate 370
solutions)] [2] which are characterized by a low melting point, T_m, 371
and high exchange current density, j_0. This indicates a strong rela- 372
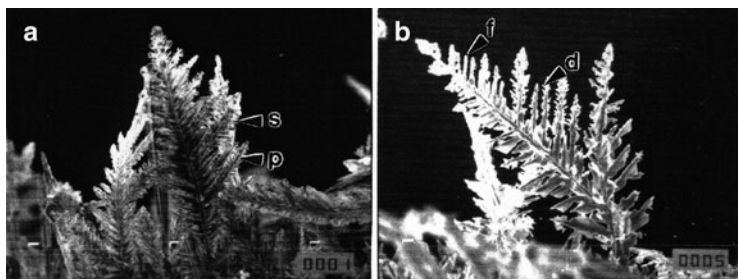tionship between nucleation type and the type of metal. 373

Fig. 2.17 Lead deposit obtained at constant overpotential deposition: (**a**) after 50 s at 75 mV, magnification: ×500 and (**b**) the same as in (**a**) but after 350 s at 0 mV, magnification: ×750 (Reprinted from [48] with permission from Elsevier and [6] with permission from Springer.)

2.3.1 The Effect of the Regime of Pulsating Overpotential on Morphology of Powder Particles

Figure 2.17a shows the lead dendrite obtained in the constant potentiostatic regime at an overpotential of 75 mV with an electrolysis time of 50 s. In all experiments for which results are presented in this section, the processes of electrodeposition were performed from solution containing 0.1 M $Pb(CH_3COO)_2$, 1.5 M $NaCH_3COO$, and 0.15 M CH_3COOH [48]. The other experimental conditions were same as for the previously analyzed solution. It is clearly visible that this dendrite possesses well-developed primary and secondary (indicated by S in Fig. 2.17a) dendrite arms as well as sharp crystallographic morphology. Figure 2.17b shows dendrites formed under the same conditions as those shown in Fig. 2.17a but obtained after a treatment at an overpotential of 0 mV with a time of 350 s. The dissolution of secondary dendrite arms occurs due to the difference in equilibrium potential between points with the different radii of curvature and the degree of dissolution varies from full dissolution (indicated by F in Fig. 2.17b) to the presence of
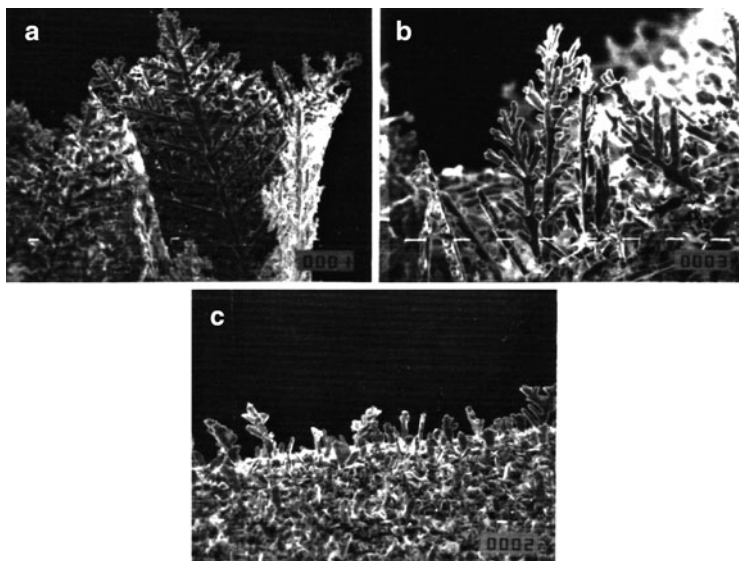
Fig. 2.18 Lead deposit obtained by square-wave pulsating overpotential at an overpotential amplitude of 75 mV with a pulse duration of 5 s and a deposition time of 120 s: (**a**) pause-to-pulse ratio: 1, ×500; (**b**) pause-to-pulse ratio: 3, ×1500, and (**c**) pause-to-pulse ratio 5, ×1000 (Reprinted from [48] with permission from Elsevier.)

secondary arm debris (indicated by D in Fig. 2.17b). Selective   393
dissolution of dendrite arms during the "off" period due to their   394
different tip radii is also seen from Figs. 2.18–2.20. So, increasing   395
the pause-to-pulse ratio p enhanced the formation of more compact   396
and less branched particles.   397

In addition to dissolution of dendrites, another phenomenon is   398
observed. The sharp crystallographic forms (Figs. 2.18a, 2.19a,   399
2.20a, c) are absent with increasing p. Also, the sharp crystallo-   400
graphic edges present in the deposited dendrites become partially or   401
well rounded after dissolution.   402

Of course, the formation of more compact and less branchy   403
powder particles in the PO electrodepositions with the increasing   404
p (at the one and the same η_A) can be ascribed to the fact that   405
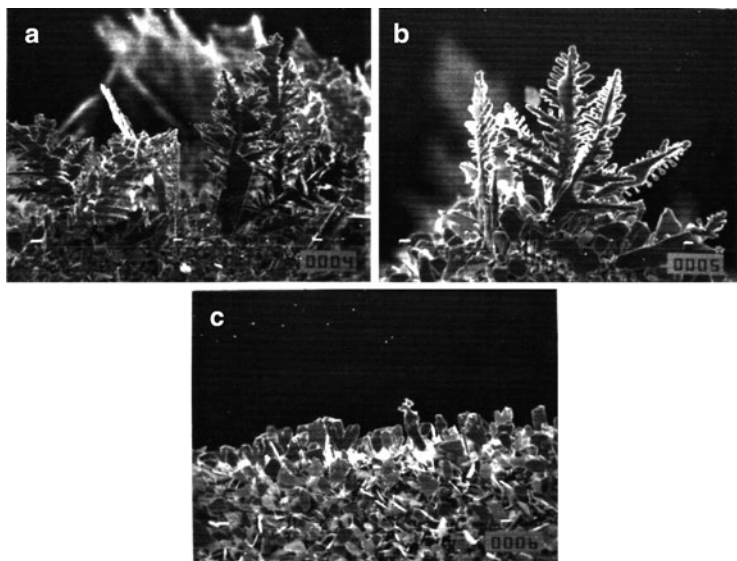
Fig. 2.19 Lead deposit obtained by square-wave pulsating overpotential at an overpotential amplitude of 75 mV with a pulse duration of 0.5 s and a deposition time of 120 s: (**a**) pause-to-pulse ratio: 1, ×500; (**b**) pause-to-pulse ratio: 3, ×1000, and (**c**) pause-to-pulse ratio: 5, ×1000 (Reprinted from [48] with permission from Elsevier and [6] with permission from Springer.)

particles with lower tip radii are dissolved faster than those with larger ones [25]. This selective dissolution is a result of the anodic current density during "off" periods, and although this current density can be neglected in relation to the cathodic one during "on" periods, its effect on the morphology of powder particles is very high. Aside from already observed the effect of the anodic current density on the morphology of silver particles, this effect was also observed during the formation of powder particles of some other metals, such as Sn [35].

This phenomenon can be qualitatively treated and Eqs. (2.2)–(2.7) are also valid for this case. Equations (2.2)–(2.7) are valid for flat electrode surfaces or protrusions with sufficiently large tip radii, where the surface energy term [25] can be neglected. If it cannot be
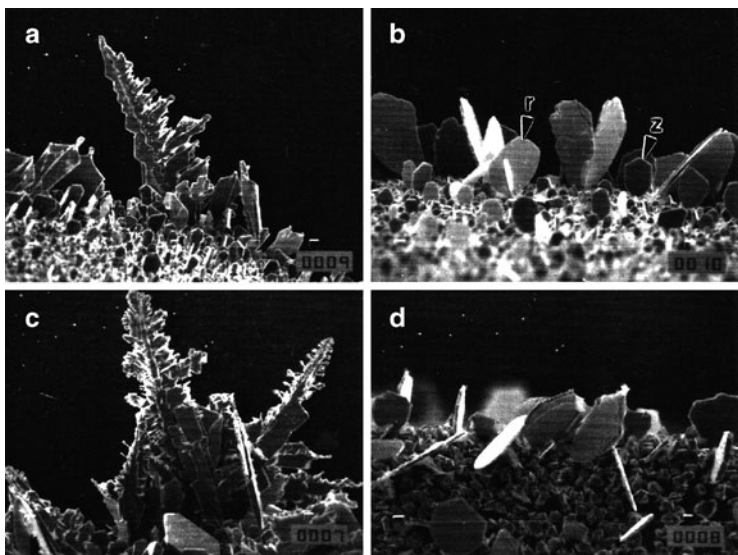
Fig. 2.20 Lead deposit obtained by square-wave pulsating overpotential at an overpotential amplitude of 75 mV with a deposition time of 120 s: (**a**) pulse duration: 0.05 s, pause-to-pulse ratio: 1, ×500; (**b**) pulse duration: 0.05 s, pause-to-pulse ratio: 3, ×1000; (**c**) pulse duration: 0.1 ms, pause-to-pulse ratio: 1, ×500; and (**d**) pulse duration 0.1 ms, pause-to-pulse ratio: 3, ×1000 (Reprinted from [48] with permission from Elsevier.)

neglected, the effect of the surface energy term on the reaction rate [33] for two electron reaction steps is described by Eq. (2.15) [31]:

$$\frac{\partial C(0,t)}{\partial x} = \frac{j_0}{nFD} \left[\left(1 - \frac{j_{av}}{j_L} \right) \exp\left(\frac{2.3\eta}{b_c} \right) - \exp\left(\frac{2\sigma V}{RTr} \right) \exp\left(-\frac{2.3\eta}{b_a} \right) \right].$$
(2.15)

The output current density, j, during pauses ($\eta = 0$) at the tip of the dendrite is presented by Eq. (2.16):

$$j = j_0 \left(1 - \frac{j_{av}}{j_L} \right) - j_0 \exp\left(\frac{2\sigma V}{RTr} \right).$$
(2.16)

423   The corresponding output current density on the flat surface is
424 given by Eq. (2.7b). The difference between the current density at the
425 tip of the dendrite and on the flat surface during the "off" period is
426 given by Eq. (2.17):

$$\Delta j = j_0 - j_0 \exp\left(\frac{2\sigma V}{RTr}\right), \tag{2.17}$$

427 if $j_{av} \approx j_L$, which is satisfied in most cases of dendrite growth.
428   Then, the change of height of surface protrusions with tip radius
429 r relative to the flat surface is given by Eq. (2.18) [34]:

$$\frac{\mathrm{d}h}{\mathrm{d}t} = \frac{V\Delta j}{nF}, \tag{2.18}$$

430 and finally, for the two electron reaction steps:

$$h = h_0 + \frac{Vj_0}{2F}\left[1 - \exp\left(\frac{2\sigma V}{RTr}\right)\right]t, \tag{2.19}$$

431 where

$$\left(m + \frac{1}{p+1}\right)T_p < t \le (m+1)T_p. \tag{2.20}$$

432   Equation (2.19) represents the height of the dendrite with tip
433 radius r as a function of time, relative to the flat surface or to the
434 protrusion with sufficiently large r. It is obvious that dendrites with
435 very low tip radii can be completely dissolved during the pause. This
436 means that the branching of dendrites can be prevented in square-
437 wave pulsating overpotential deposition. Obviously, the larger p,
438 the greater the degree of dissolution, as follows from Eq. (2.20).
439 The effect is more pronounced if η_A remains constant and p increases,
440 as seen from Figs. 2.18–2.20.
441   The effect of the "off" period on the micromorphology of metal
442 powder particles can also be seen by the following analysis of lead
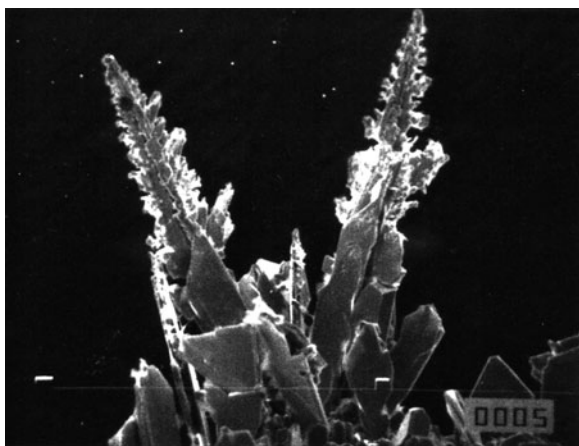443 surface morphology. The lead dendrites obtained in the PO

Fig. 2.21 Lead deposit obtained in constant overpotential deposition at 30 mV with a deposition time of 120 s. Magnification: ×750 (Reprinted from [48] with permission from Elsevier.)

electrodeposition using overpotential amplitude of 75 mV and $p = 1$ at frequencies of 10 and 5,000 Hz (Fig. 2.20a, c) are more similar to those obtained at constant overpotential of 30 mV (Fig. 2.21) than those obtained at 75 mV (Fig. 2.17a), what can be explained as follows.

The average current density in the pulsating overpotential deposition can be obtained from [34]

$$j_{av} = \frac{j_0}{p+1}\left[\left(1 - \frac{j_{av}}{j_L}\right)\exp\left(\frac{2.3\eta_A}{b_c}\right) - p\frac{j_{av}}{j_L}\right], \qquad (2.21)$$

if the anodic current density is neglected during overpotential pulses, and the overpotential amplitude can then be obtained in the form

$$\eta_A = \frac{b_c}{2.3}\ln\frac{j_{av}}{j_0} + \frac{b_c}{2.3}\ln\left(p + 1 + \frac{pj_0}{j_L}\right) + \frac{b_c}{2.3}\ln\left(\frac{1}{1 - j_{av}/j_L}\right). \qquad (2.22)$$

453   The third term in Eq. (2.22) corresponds to bulk diffusion control.
454 It remains constant for a determined average current density regard-
455 less of the pause-to-pulse ratio, whereas the second term, which with
456 the first one represents the activation part of the overpotential, increases
457 with increasing p. In this way the ratio between overpotential corres-
458 ponding to bulk diffusion control and activation overpotential can be
459 reduced to the value corresponding to the deposition at lower over-
460 potentials in the constant overpotential regime. So, it can be expected
461 that deposits obtained at η_A in pulsating regimes ($p > 0$) are more
462 similar to those obtained at lower overpotentials than at η_A in the
463 constant overpotential regime ($p = 0$).

464   On the other hand [32], the overpotential and current density on
465 the tips of growing dendrites inside the diffusion layer are related by:

$$j_d = j_0 \frac{h}{\delta} \exp\left(\frac{2.3\eta_A}{b_c}\right) \tag{2.14}$$

466 and

$$j_{d,av} = j_0 \frac{h}{\delta(p+1)} \exp\left(\frac{2.3\eta_A}{b_c}\right) \tag{2.23}$$

467 in the constant and pulsating overpotential regimes, respectively.
468 This means that dendritic growth is reduced in pulsating overpotential
469 deposition. This is the second reason why dendrites, or powder
470 particles, obtained in pulsating overpotential deposition are more simi-
471 lar to those obtained at lower overpotentials than to those obtained at
472 overpotential amplitude in constant overpotential deposition.

473   The effect of the frequency of pulsation on the morphology is also
474 illustrated by Figs. 2.18–2.20. It seems that under deposition at high
475 frequencies (Fig. 2.20) more pronounced anodic dissolution during the
476 pause occurs compared with the deposition at lower frequencies
477 (Figs. 2.18 and 2.19), which leads to a formation of less dendritic deposit.

478   The difference between the morphologies obtained at lower and
479 higher frequencies can be explained as follows. At sufficiently high
480 frequencies the current response to the input overpotential is given by
481 Eq. (2.7), while at lower frequencies it is given by

2 Morphology of Different Electrodeposited Pure Metal Powders

$$
j = \begin{cases}
j_0 \dfrac{C(0,t)}{C_0} \quad \exp\left(\dfrac{2.3\eta_{\mathrm{A}}}{b_{\mathrm{c}}}\right) - j_0 \exp\left(-\dfrac{2.3\eta_{\mathrm{A}}}{b_{\mathrm{a}}}\right) \\
\qquad\qquad \text{for} \quad mT_{\mathrm{p}} < t \leq \left(m + \dfrac{1}{p+1}\right)T_{\mathrm{p}} \qquad (a)\,. \\
j_0\left(\dfrac{C(0,t)}{C_0} - 1\right) \text{for} \quad \left(m + \dfrac{1}{p+1}\right)T_{\mathrm{p}} < t \leq (m+1)T_{\mathrm{p}} \ (b)
\end{cases}
$$
$$(2.24)$$

The anodic current during the "off" period is constant and can have significant value at sufficiently high frequencies [Eq. (2.7b)]. At lower frequencies [Eq. (2.24b)], when $C(0,t)$ becomes equal to C_0 the anodic current is zero and the average anodic current during the "off" period can be considerably lower than in the previous case.

Hence, the change of morphology of the deposit can be the indicator of the frequency at which the surface concentration becomes independent of time in pulsating overpotential deposition. This happens at a frequency of 10 Hz as seen from Figs. 2.19 and 2.20.

The formation of silver and lead powdered deposits from nitrate solutions was accompanied by the absence of hydrogen evolution as the second reaction. In the case of silver, the reason for it is the fact that the reversible potential of silver electrode is sufficiently positive to avoid hydrogen evolution reaction. In the case of lead, hydrogen evolution is extremely slow process, and then, hydrogen evolution is negligible at overpotentials at which lead was electrodeposited. The extremely high exchange current densities of these metals permit the formation of dendrites at low overpotentials, and very pronounced effect of selective dissolution during the "off" periods in the pulsating overpotential regime in both the millisecond and second range was observed.

2.4 Cadmium

Cadmium also belongs to the group of normal metals which are characterized by the large exchange current densities. In the case of cadmium, hydrogen evolution is also a slow process and this fact enables the analysis of the formation of cadmium dendrites without the effect of any parallel process.
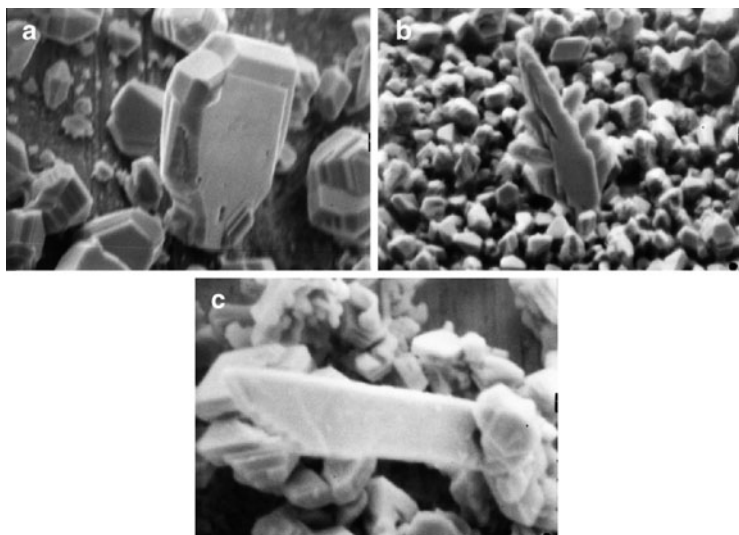
Fig. 2.22 Precursors of cadmium dendrites obtained by electrochemical depositions at overpotentials, η, of: (**a**) $\eta = 50$ mV; deposition time, $t = 2$ min; magnification: ×5000; (**b**) $\eta = 110$ mV; $t = 2$ min; ×3000; and (**c**) $\eta = 130$ mV; $t = 3$ min; ×9000 (Reprinted from [53] and [54] with permission from Elsevier and [6] and [47] with permission from Springer.)

Precursors of cadmium dendrites [47] obtained by the processes of electrochemical deposition from 0.1 M CdSO$_4$ in 0.50 M H$_2$SO$_4$ onto cadmium wire electrodes at different overpotentials are shown in Fig. 2.22. It is obvious that further growth of the dendrite precursors shown in Fig. 2.22 leads to the formation of 2D dendrites (Fig. 2.23). Around the tips of dendrite precursors, as well as around the tips of dendrites, spherical or cylindrical diffusion control can occur, which is in good agreement with the requirements of the mathematical model.

There is an induction period before initiation of dendritic growth [25, 33, 49, 50]. During this induction period, dendrite precursors are formed by the growth of suitable nuclei. According to Pangarov and Vitkova [51, 52] the orientation of nuclei is related to the overpotential used. The effect of overpotential of electrodeposition on the shape of cadmium dendrites is illustrated in Fig. 2.23.

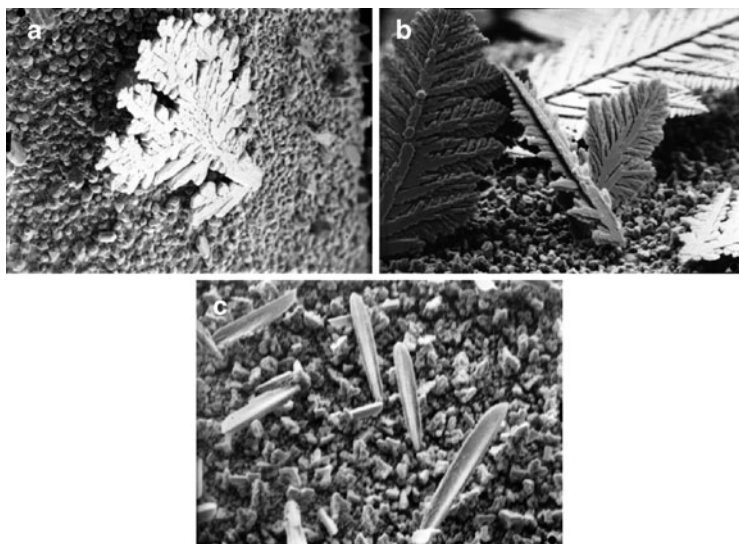**Fig. 2.23** Cadmium dendrites obtained at overpotentials, η, of: (**a**) $\eta = 50$ mV; $t = 10$ min; $\times 200$; (**b**) $\eta = 110$ mV; $t = 2$ min; $\times 400$; and (**c**) $\eta = 130$ mV; $t = 3$ min; $\times 1000$ (Reprinted from [53] with permission from Elsevier and [6] and [47] with permission from Springer.)

Most of the data concerning Co, Fe and Ni powders electrode- position   523
are summarized in Chapter XVIII of the book "Electrodeposition of   524
Powders from Solutions," by Calusaru [55].   525

2.5   The Iron-Group Metal Powders   526

According to Calusaru [55] some information on electrodeposition of   527
Co powder is available in patents [56] as well as in reviews [57].   528
Unfortunately these references are from 1932 and there are no data   529
about the morphology of powder particles, since then there are no   530
published data about electrodeposition of Co powder. Only two   531
micrographs of Co powder, showing that the particles are very fine   532
agglomerates, are presented in the Metallographic Atlas of Powder   533

534 Metallurgy [58], but the procedure of their production is not
535 mentioned and it is stated that their typical application is for hard
536 metal production.

537   Contrary to the limited data for Co and Ni powders electrodeposi-
538 tion, the highest number of 71 references for Fe powder electrodepo-
539 sition exist in the book of Calusaru [55]. In this introduction only the
540 most important ones are cited.

541   Because of its application in the manufacturing of porous metallo-
542 ceramic bearings, of friction materials, parts for machinery, various
543 alloys, in chemical industry, in manufacture of rechargeable batteries,
544 etc., Fe powder is an important industrial product [55]. Significant
545 amount of Fe powder is produced by electrochemical technique and
546 20% of electrodeposited Fe powders have to be blended with Fe
547 powders produced by other procedures. The main advantage of
548 electrodeposited Fe powder is its volumetric mass (1.5–2.2 g cm^{-2})
549 and its suitability for pressing, due to dendritic particle shape.

550   Generally speaking, in most of the electrolytes for Fe powder
551 electrodeposition fragile deposits were obtained and transformed
552 into powders by removal from the cathode surface and subsequent
553 grinding [59–70]. Very few high purity Fe powders were obtained by
554 electrodeposition. Usually these powders contain certain amount of
555 oxides, mainly due to powder oxidation during the washing and
556 drying procedure.

557   Three types of electrolytes were used for Fe powder electrodepo-
558 sition (1) electrolytes based on sulfate salts [59–63]; (2) electrolytes
559 based on chloride salts [65–69]; and (3) alkaline electrolytes: reduc-
560 tion of $Fe(OH)_2$ suspension in alkaline media [71]; formation of
561 $Fe(OH)_3$, and its reduction from the suspension of Fe_3O_4 in alkaline
562 solution [70].

563   Because of the possibility for $Fe(OH)_2$ or $Fe(OH)_3$ formation the
564 suggested pH values for the electrolytes are pH < 3.

565   An interesting method for producing very fine Fe powder
566 by the electrolysis in a two-layer electrolytic bath using a hydrocar-
567 bon solvent from an oil refining fraction as an upper organic
568 layer has also been suggested [72]. It was also shown that in the
569 presence of chelating agents, fine, nondendritic Fe powders could
570 be obtained [73].

Two types of electrolytes for Ni powder electrodeposition were investigated: acid electrolytes [74–82] and ammoniacal electrolytes [74, 77, 83]. For acid electrolytes it is characteristic that the increase of current density and decrease of nickel ion concentration in solution cause a lowering of powder fragility. The powder is free from oxides and basic salts and dry powder could be stored in a dry place indefinitely without oxidation or structure change [74–82]. Characteristic of ammoniacal electrolytes is that the increase of ammonia concentration cause disperse and pure (without hydroxide impurities) deposit formation consisting of dark nickel particles of 4–10 μm and of larger particles of about 400 μm [74, 77, 83].

The influence of pulsating and reversing current regime on the Ni powder electrodeposition was investigated in the paper of Pavlović et al. [84]. It is found that the increase of frequency of pulsating current induces a decrease in particle size, while in the case of reversing current regimes the size of powder particles increase with increasing average current density.

2.5.1 Characterization of the Polarization Curves for Co, Fe, Ni Powders Electrodeposition

It is well known that the electrodeposition of the iron group metals (Co, Fe, Ni) occurs with simultaneous hydrogen evolution [85–89]. In such a case it is practically impossible to determine the diffusion limiting current density for their electrodeposition from the polarization curves (contrary to the case of the electrodeposition of Ag, Cu, Pd, etc) and define the beginning of powder formation expressed with the increase of current density over the diffusion limiting current density, corresponding to the process of simultaneous hydrogen evolution. To obtain correct polarization curves for the electrodeposition of these systems it is necessary to apply IR drop compensation technique. In all our cases the current interrupt technique was used, while polarization curves were recorded onto glassy carbon electrode.
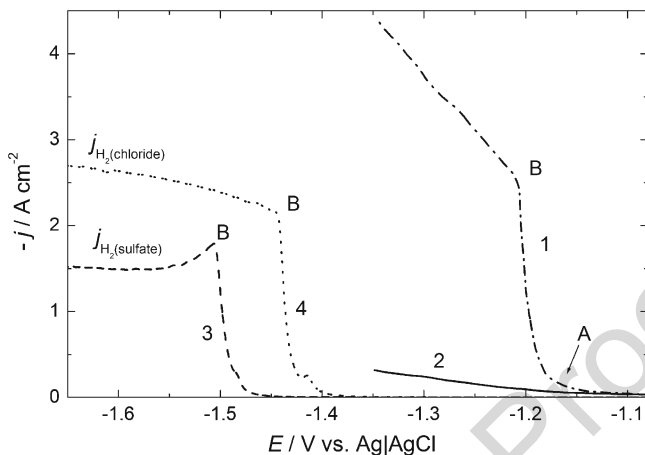
Fig. 2.24 Typical polarization curves for the electrodeposition of Co powder from ammonium sulfate–ammonium hydroxide supporting electrolyte with (1) and without (2) IR drop correction. Polarization curves for hydrogen evolution in different supporting electrolytes are also presented in the figure (*curves* 3 and 4) (Reprinted from [90, 91] with the permission of Elsevier.)

603   Polarization curves were recorded in a three-compartment
604 standard electrochemical cell at the room temperature. The sweep
605 rate was 1 mV s^{-1} and current interrupt was applied at each 0.5 s.
606 The platinum foil counter electrode and the reference—saturated
607 silver/silver chloride, Ag|AgCl—electrode were placed in separate
608 compartments. The working electrode was glassy carbon disc
609 ($d = 0.3$ cm) placed parallel to the counter electrode.

610   Typical polarization curves with (1) and without IR drop correc-
611 tion (2) are presented in Fig. 2.24. While recording polarization
612 curves with and without IR drop correction for all investigated
613 alloy powders electrodeposition, almost identical difference between
614 curves with (1) and without IR drop correction (2) for all supporting
615 electrolytes, as well as for all investigated systems is obtained.
616 In Fig. 2.24 is shown an example for Co electrodeposition from
617 ammonium sulfate containing supporting electrolyte [90, 91].

618   As can be seen after IR drop correction (dash-dot line—1) signifi-
619 cantly different current response is obtained than the one measured

without IR drop correction (solid line—2), being characterized by a 620
sudden increase of current density at the commencement of the elec- 621
trodeposition process. As far as the electrodeposition started, hydrogen 622
evolution also started and the processes of all metal electrodeposition 623
were accompanied by hydrogen evolution in the whole range of 624
investigated potentials. As a consequence, extremely high current 625
densities were recorded (since at the pH 9.2–9.5 hydrogen is evolving 626
from water molecules) and accordingly correction for IR drop caused 627
significant change in the shape of the polarization curves. At the same 628
time it is important to note that because of intensive hydrogen evolution 629
already at the commencement of the process of the electrodeposition, 630
Co powder formation took place at current densities as low as 631
0.3 A cm^{-2} (low in comparison with the maximum current density of 632
3–6 A cm^{-2}). The characteristic for all curves is that after sudden 633
increase of current (in this case at about -1.17 V—point A) additional 634
inflection point appeared on the polarization curves (B) at the potential 635
of about -1.21 V with further change of current density showing linear 636
increase with the potential. 637

2.5.1.1   Polarization Curves for Hydrogen Evolution onto 638
Glassy Carbon Electrode 639

As shown in Fig. 2.24 in a pure supporting electrolytes (1 M 640
$(NH_4)_2SO_4 + 0.7 NH_4OH$ or 1 M $NH_4Cl + 0.7 NH_4OH$) polarization 641
curves for hydrogen evolution, corrected for IR drop, are different 642
than those for metal or alloy electrodeposition, and their shapes and 643
positions on the potential scale depend on the anions present in a 644
supporting electrolyte. In both electrolytes the increase of current 645
density corresponding to the hydrogen evolution onto glassy carbon 646
electrode (3 and 4) is seen to take place at more negative potentials 647
than in the case of metal or alloy electrodeposition. It is interesting to 648
note that the overpotential for hydrogen evolution in sulfate 649
containing supporting electrolyte is for about 0.1 V higher than that 650
in chloride containing supporting electrolyte. Such a behavior is a 651
clear indication that the processes of Co electrodeposition catalyze 652
the reaction of hydrogen evolution in both supporting electrolytes. 653

654   Concerning the shape of both polarization curves for hydrogen
655 evolution it appears that such shape is a consequence of the so called
656 electrode effect [92–97]. This phenomenon is connected with the
657 hydrogen bubble formation at high current densities, so that at the
658 inflection point B the formation of bubbles becomes the rate limiting
659 step of the electrochemical process [96, 97]. Accordingly, the shape
660 of the polarization curves for iron group metal and their alloy elec-
661 trodeposition is also defined by the process of bubble formation since
662 the current density for hydrogen evolution in all cases amounts
663 to 70–85% of total current density.

2.5.1.2   Current Efficiency Determination

665 Taking into account that simultaneous hydrogen evolution occurs
666 in all cases, it was necessary to determine the current density for
667 hydrogen evolution (j_H), subtract it from the measured (corrected
668 for IR drop) current density values (j_{tot}) given in Fig. 2.25a to obtain
669 current densities for powders electrodeposition (in this case Co pow-
670 der, j_{Co}). Hence, several values of current density on the polarization
671 curve for Co powder electrodeposition were chosen and the volume of
672 evolved hydrogen was determined in the burette. The current for
673 hydrogen evolution (○) was obtained using the equation [98]

$$I_{H_2} = \frac{nFV}{tV_n} = \frac{nF}{V_n} \times \frac{V}{tT} = 2.3522 \times 10^3 \times \frac{V}{tT}, \qquad (2.25)$$

674 where V—experimentally determined volume of the evolved hydro-
675 gen at P_{at} and $T = 298$ K corrected to the normal conditions ($P^{\ominus}$ and
676 $T = 273$ K); t—time of hydrogen evolution under constant current;
677 V_n—volume of 1 mol of hydrogen at normal conditions
678 (22.4 dm^3 mol^{-1}); n—number of exchanged electrons, and F—
679 Faraday's constant. Using this procedure polarization curve
680 corresponding to Co powders electrodeposition (△) was obtained.
681   The current efficiency (•) for the electrodeposition process was
682 obtained from the relation

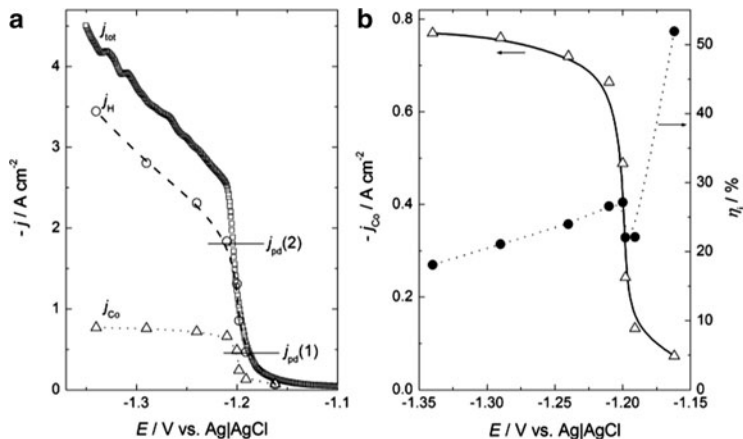**Fig. 2.25** (**a**) Polarization curve for the electrodeposition of Co powder after IR drop correction (j_{tot}), polarization curve for hydrogen evolution (j_H), and polarization curve for Co powder electrodeposition (j_{Co}) after subtraction of the current density for hydrogen evolution. (**b**) Polarization curve for Co powder electrodeposition (j_{Co}) and corresponding current efficiency curve (η_j) (Reprinted from [90, 91] with the permission of Elsevier.)

$$\eta_j(\%) = \frac{j_{Co-Ni}}{j_{tot}} \times 100 = \frac{j_{tot} - j_H}{j_{tot}} \times 100. \qquad (2.26)$$

Corresponding values are presented in Fig. 2.25b.   683

As can be seen already at the beginning of the deposition process   684
significant amount of hydrogen is evolving, causing the value of the   685
current efficiency of about 52%. At more negative potentials this   686
value decreases to about 20–25%, with the sharp decrease taking   687
place in the region of the sharp increase in current density.   688

All powder samples for XRD analysis and morphology   689
investigations were electrodeposited at the room temperature in the   690
cylindrical glass cell of the total volume of 1 dm^3 with cone-shaped   691
bottom of the cell to collect powder particles in it. Working electrode   692
was a glassy carbon rod of the diameter of 5 mm, with the total   693
surface area of 7.5 cm^2 immersed in the solution and placed in the   694
middle of the cell. Cylindrical Pt–Ti mesh placed close to the cell   695

696 walls was used as a counter electrode providing excellent current
697 distribution in the cell.
698   In all cases certain, small amount of disperse deposit remained on
699 the glassy carbon electrode, while only powder particles that were
700 detached from the electrode surface and collected at the cone-shaped
701 bottom of the cell were analyzed.

2.5.2   Electrodeposition of Co Powder

703 Cobalt powder was electrodeposited from the solutions containing
704 either sulfate or chloride anions.

2.5.2.1   Electrodeposition of Co Powder from Sulfate Electrolyte

707 The composition of the electrolyte was 1M $(NH_4)_2SO_4$ + 0.7 M
708 NH_4OH + 0.1 M $CoSO_4$, pH 9.5. Polarization curves were recorded
709 on the glassy carbon disc by the procedure explained in Sect. 2.2.
710 The powders for SEM and XRD analyses were electrodeposited at
711 two constant current densities (see Fig. 2.25a): $j_{pd}(1) = -0.50$ A
712 cm^{-2} and $j_{pd}(2) = -1.85$ A cm^{-2}.
713   The polarization curve and the corresponding current efficiency
714 potential dependence are presented in Fig. 2.25b. The process of Co
715 electrodeposition commences at about -1.10 V with the second
716 inflection point being placed at -1.20 V. The curve for Co powder
717 electrodeposition (j_{Co}) is characterized with well-defined current
718 density plateau in the potential range between -1.20 V and -1.35 V,
719 indicating that at potentials more negative than -1.20 V diffusion
720 limiting current density for Co powder electrodeposition is reached in
721 Fig. 2.25a. The current efficiency (η_j), obtained using equation (2.26), is
722 seen to decrease sharply from about 52% to about 20% in the potential
723 range of sharp increase of current density on the polarization curve j_{Co}
724 vs. E in Fig. 2.25b. At potentials more negative than -1.20 V, η_j vs. E
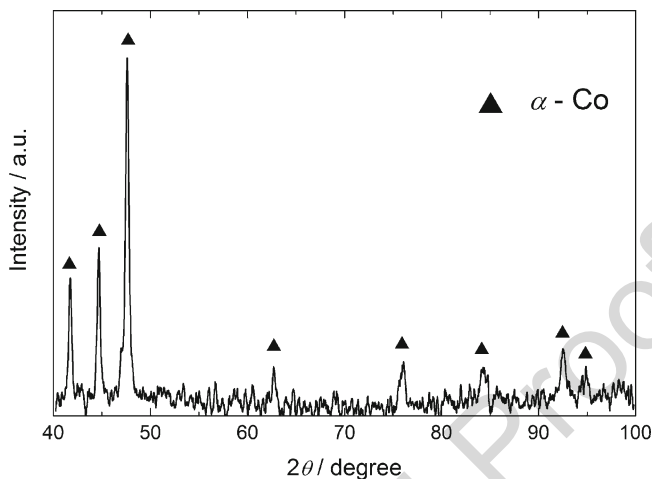725 dependence slightly decreases from about 27% to about 20%.

Fig. 2.26 X-ray diffraction pattern of electrodeposited cobalt powders (Reprinted from [99] with the permission of Springer-Verlag.)

X-ray diffraction pattern for Co powder samples electrodeposited either with $j_{pd}(1)$ or $j_{pd}(2)$, from sulfate or chloride electrolytes, is shown in Fig. 2.26. As can be seen the powder consists only of the hexagonal close-packed α-cobalt phase with the lattice parameters of $a = 2.5007$ Å and $c = 4.0563$ Å. No hydroxide or oxide impurities were detected [99].

In the case of Co powder electrodeposition at lower current density ($j_{pd}(1) = -0.50$ A cm^{-2}), generally two types of agglomerates are detected [99]:

1. Dendrite particles varying in the size from about 5 μm to about 50 μm, as shown in Fig. 2.27a.
2. Different types of agglomerates varying in the size from about 100 μm to about 500 μm, as it is shown in Fig. 2.27b–d. These agglomerates can further be divided into three groups:

   (a) Compact agglomerates of the size of about 200 μm to about 500 μm, composed of smaller agglomerates of the size of about 20 μm to about 50 μm, Fig. 2.27b. These agglomerates are characterized with the presence of deep cylindrical

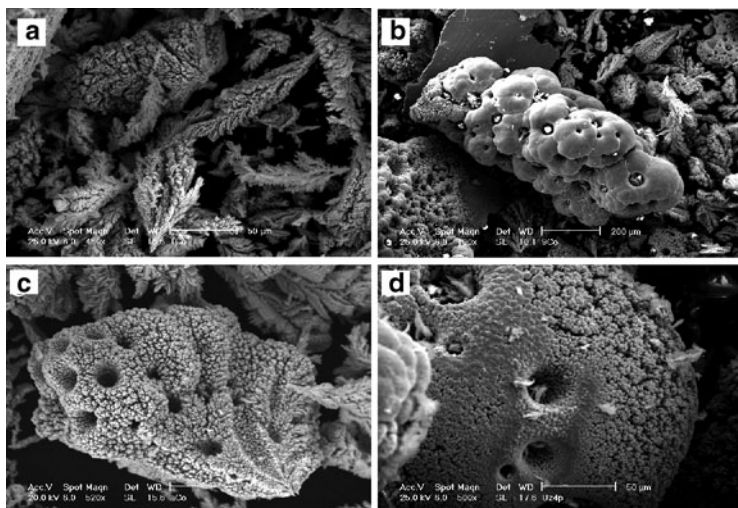**Fig. 2.27** Typical particles detected in the electrodeposited cobalt powder (Reprinted from [99] with the permission of Springer-Verlag.)

cavities and fern-like dendrites formed on the bottom of most of the cavities.

(b) Spongy-like agglomerates of different shapes varying in size from about 100 μm to about 200 μm with the fern-like dendrites also formed on the bottom of most of the cavities, Fig. 2.27c.

(c) Balls of the size of about 200 μm containing deep cavities with the fern-like dendrites formed on the bottom of most of the cavities and more or less dense cauliflower structure on the surface of these balls, as shown in Fig. 2.27d.

In Figs. 2.28a–d and 2.29a, b cross sections of some of the agglomerates detected in the Co powder deposit are shown.

As can be seen they are in good agreement with the SEM results: Fig. 2.28b ball-like particles; Fig. 2.28c spongy particles; Fig. 2.28d compact agglomerates. Although for Co powder different types of agglomerates are present, it is quite obvious that all Co powder
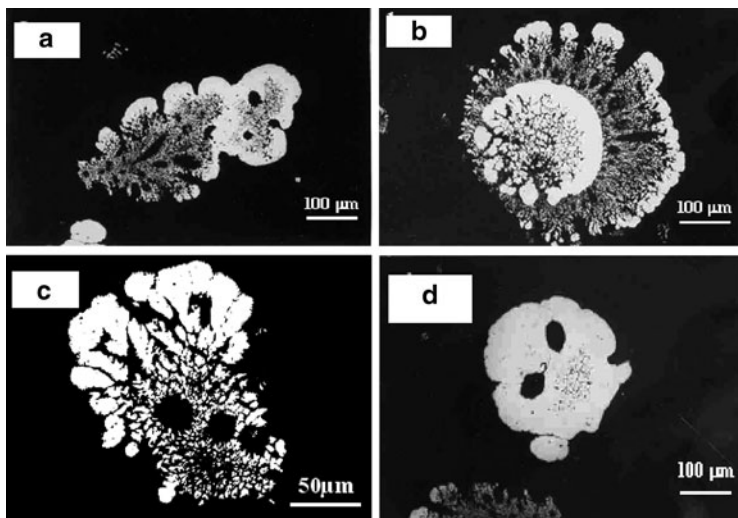
Fig. 2.28 Cross sections of some of the agglomerates detected in the Co powder deposit (Reprinted from [99] with the permission of Springer-Verlag.)
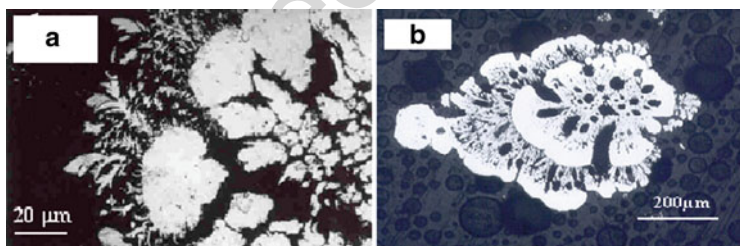

Fig. 2.29 Cross sections of some of the agglomerates detected in the Co powder deposit (Reprinted from [99] with the permission of Springer-Verlag.)

agglomerates are characterized with the presence of large number of cavities. A common characteristic of these cavities for all types of agglomerates (Fig. 2.27) is the presence of small fern-like dendrites on the bottom of most of the cavities.

2.5.2.2 Mechanism of Co Powder Electrodeposition

Considering cross sections of some of the agglomerates detected in the Co powder deposit [99], Figs. 2.28 and 2.29, it appears that they are all different, not only because different types of agglomerates have been detected but also because some pictures represent cross sections of the agglomerate parallel to the line of its growth (Fig. 2.28a), while some pictures represent cross sections of the agglomerate normal to the line of its growth (Fig. 2.28b–d). It has already been explained in the literature [100] that in the case of dendrite particles, depending on their length, it is possible that the morphology of the dendrite changes from disperse one to a compact one, as shown in Fig. 2.28a. This agglomerate seems to grow from the left to the right side.

With the time of growth the disperse agglomerate is branching in different directions and at the tip of each branch spherical diffusion is taking over the planar one, providing conditions for the growth of compact deposit as a consequence of the decrease of the local current density on the tip of each branch. After some time, these branches form compact deposit all over the agglomerate surface and the same agglomerate further grows as a compact one (right side of the particle), until it falls off from the electrode surface. In Fig. 2.28b it is most likely that a compact part of the agglomerate represents the picture of the cross section normal to the line of its growth. Depending on the way of growth, the moment of detaching agglomerate from the electrode surface and the position at the electrode surface where some agglomerate started to grow, different shapes of agglomerates are obtained (Fig. 2.28a–d), but all of them show the same characteristic of transforming disperse into compact deposit with increasing their size.

AU3

A special case is the formation of the balls of the size from about 200 μm containing deep cavities with the fern-like dendrites formed on the bottom of cavities and more or less dense cauliflower structure on the surface of these balls, Fig. 2.27d. The cross section of such agglomerate is shown in Fig. 2.28b. For some reasons this agglomerate started to grow as a ball, again starting from disperse (in the middle) and finishing with compact deposit at the surface for a reason

already explained. After some time of the growth of compact deposit 800
the conditions for planar diffusion were restored causing the forma- 801
tion of dendrites all over the ball surface. It should be noted that at the 802
same time there was a local increase of overpotential due to reduction 803
of the active surface area as a result of compact deposit formation. 804
Dendrites were growing normal to the ball surface, and again after 805
some time spherical diffusion took over the control of the planar one 806
and dendrites started transforming into compact deposit. Since 807
dendrites were not dense, they were not able to form compact deposit 808
all over the agglomerate surface when the agglomerates detached 809
from the electrode surface. 810

A cross section of one of the agglomerates parallel to the line of its 811
growth is shown in Fig. 2.29b. As can be seen, in accordance with the 812
previous statement, after the first front of compact deposit has been 813
formed, disperse deposit started to grow and for the same reasons its 814
growth finished as a compact deposit at the moment when this 815
agglomerate detached from the electrode surface. 816

It is necessary to note that almost all morphological forms 817
presented in this chapter can be explained by the above discussion, 818
being dependent on the stage of the agglomerates, i.e., the moment 819
when they detached from the electrode surface. It is most likely that 820
the form presented in Fig. 2.30 should be considered as the initial 821
stage of the growth of a second generation of dendrites, clearly 822
detected on a cross section of ball-like particles presented in 823
Fig. 2.29a. 824

Quite unique feature of all agglomerates detected in Co powder 825
deposit is the presence of deep cavities on their surfaces and the fern- 826
like dendrites on their bottom for most of the cavities. This is 827
illustrated in Fig. 2.27b for compact agglomerates and in Fig. 2.27d 828
for ball-like agglomerates. The most interesting one is the cavity 829
detected in the ball-like agglomerates. More detailed micrograph 830
for such cavity is shown in Fig. 2.31. 831

It is most likely that these cavities are the consequence of hydro- 832
gen bubble formation, preventing deposition inside the cavity. Once 833
the bubble is liberated, the conditions for the growth of fern-like 834
dendrites are fulfilled at the bottom of the cavity due to current 835
distribution and restored planar diffusion. Since this agglomerate is 836
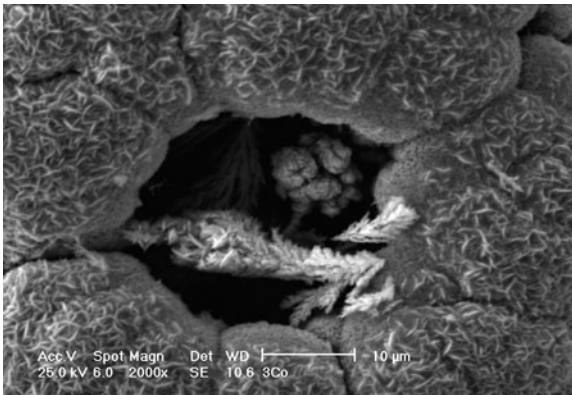not dense, crystals of different size can be seen in the cavity, with less 837

Fig. 2.30 SEM micrograph of the surface of compact agglomerate with the initial stage of the growth of a second generation of dendrites (Reprinted from [99] with the permission of Springer-Verlag.)

Fig. 2.31 SEM micrograph of the cavity detected on the ball-like agglomerate (Reprinted from [99] with the permission of Springer-Verlag.)

838 dense ones placed at the bottom and more dense ones placed close to
839 the top of the cavity. We believe that such distribution of crystals is
840 the consequence of current distribution over the hydrogen bubble,
841 while at the moment of bubble liberation fern-like dendrite starts

growing at the bottom of cavity in the same way as the dendrite precursors in the diffusion layer of the macroelectrode [101]. At that moment spherical diffusion is restored at the edges of cavity and compact deposit is obtained all around the cavity.

Concerning spongy deposits, it should be emphasized here that in comparison with other morphologies, traditionally called spongy, presented in the literature [47, 102] so far, the morphology of particles shown in Fig. 2.27c represents the real spongy deposit and that such similarity with the sponge has never been presented so far.

The morphology of Co powder electrodeposited at higher current density ($j_{pd}(2) = -1.85$ A cm^{-2}) is much more uniform in comparison with the morphology of Co powder electrodeposited at a lower current density.

Independently of the substrate (Co powders were electrodeposited onto GC, Co, and Ni electrodes) all agglomerates possessed spongy-like shapes, some of them being bigger (about 600 μm, Fig. 2.32a), while most of the agglomerates were of the order of 100–200 μm, Fig. 2.32b, c. The best sample for the formation of such agglomerates is presented in Fig. 2.32c. They start growing as dendrites (marked with arrow ←1) and after some time, for the reasons explained earlier, their surfaces become compact and characterized with the presence of two types of cavities (as a consequence of hydrogen bubbles formation on the agglomerate surfaces): cone-shaped ones (marked with arrow 2→) and cylindrical ones (marked with arrow ←3, identical to those obtained for Co powders electrodeposited at lower current density, $j_{pd}(1) = -0.50$ A cm^{-2}). It is interesting to note that fern-like dendrites were not formed on the bottom of cylindrical cavities, indicating that the agglomerates were detached from the electrode surface before the liberation of hydrogen bubbles formed on their surfaces. Hence, the electrolyte did not enter the cavities providing conditions for planar diffusion inside the cavity and the growth of fern-like dendrites. This is reasonable to expect since the time for agglomerates detaching should be much shorter for more intensive hydrogen evolution at $j_{pd}(2)$.

Considering Fig. 2.32 it can be concluded that most of the agglomerate surfaces are covered with very flat nodular endings. By the investigation of these surfaces at higher magnification it is discovered
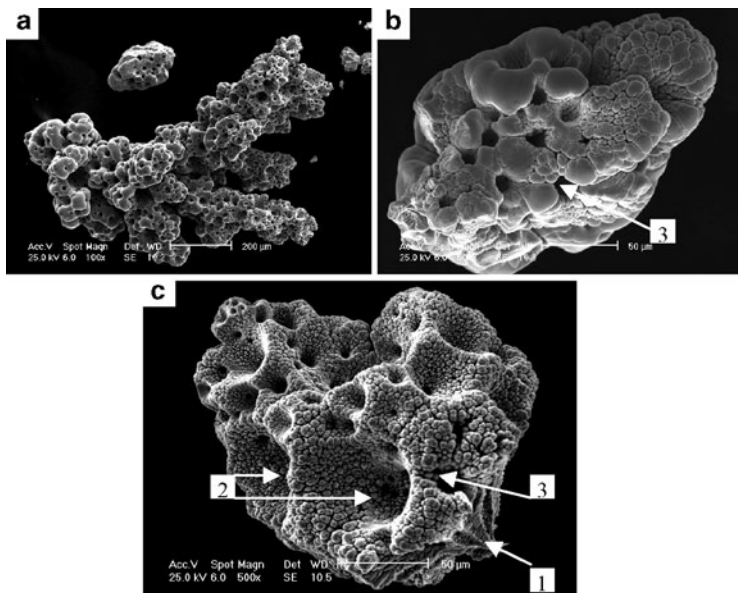
Fig. 2.32 SEM micrographs of the agglomerates electrodeposited at high current density

that these flat surfaces are actually composed of very thin (about 0.1 μm) and about 1 μm long crystals of Co, as shown in Fig. 2.33.

2.5.2.3 Electrodeposition of Co Powder from Chloride Electrolyte

The composition of the electrolyte was 1M $NH_4Cl + 0.7$ M $NH_4OH + 0.1$ M $CoCl_2$, pH 9.4. Polarization curves were recorded on the glassy carbon (GC) and Co discs. The powders for SEM and XRD analyses were electrodeposited at a constant current density of -2.00 A cm^{-2} onto GC electrode and -0.77 A cm^{-2} onto Co electrode.

The polarization curve and the corresponding current efficiency potential dependence recorded onto GC electrode are presented in Fig. 2.34. The shape of the polarization curve in Fig. 2.34a is
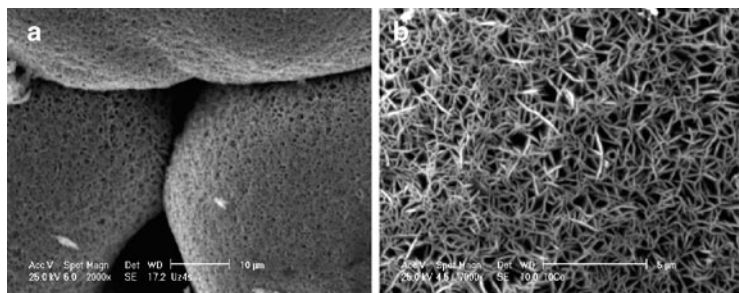
Fig. 2.33 Structure of the flat nodular endings detected on the surfaces of agglomerates electrodeposited at high current density. The same structure was detected on compact agglomerates electrodeposited at low current density
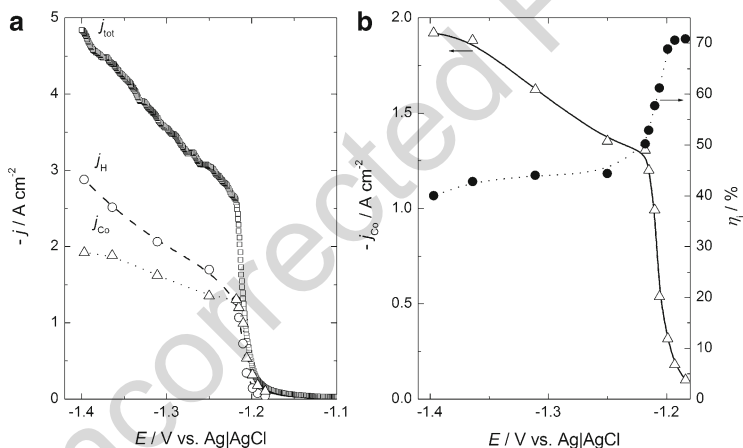

Fig. 2.34 (**a**) Polarization curve for the electrodeposition of Co powder after IR drop correction (j_{tot}), polarization curve for hydrogen evolution (j_H) and polarization curve for Co powder electrodeposition (j_{Co}) after subtraction of the current density for hydrogen evolution. (**b**) Polarization curve for Co powder electrodeposition (j_{Co}) and corresponding current efficiency curve (η_j) (Reprinted from [90, 91] with the permission of Elsevier.)

identical to the one recorded for Co powders electrodeposition from 892
sulfate electrolyte (Fig. 2.25a). As can be seen in Fig. 2.34 the 893
process of Co electrodeposition commences at about -1.10 V with 894
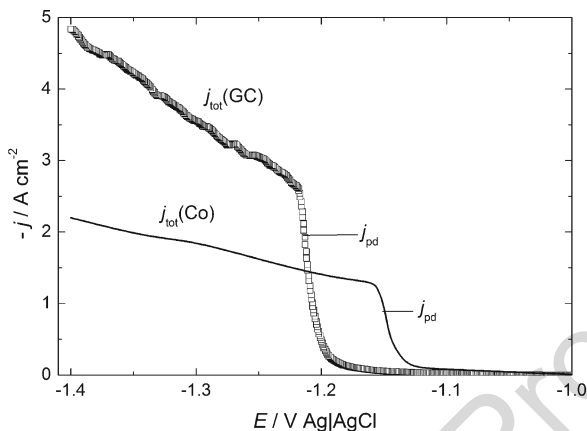the second inflection point being placed at -1.21 V. The curve for Co 895

Fig. 2.35 Polarization curves for the electrodeposition of Co powder after IR drop correction (j_{tot}) recorded onto GC electrode (j_{tot}(GC)) and onto Co electrode (j_{tot}(Co))

896 powder electrodeposition (j_{Co}) in this case is not characterized
897 with well-defined current density plateau in the potential range
898 between -1.21 V and -1.40 V as was in the case sulfate electrolyte,
899 Fig. 2.25a. A linear increase of the current density for Co powder
900 electrodeposition (j_{Co}) is most likely due to the increase of real
901 surface area of the electrode covered with compact deposit and/or
902 different intensity of hydrogen evolution in this electrolyte.
903 The current efficiency (η_j) is seen to decrease sharply from about
904 70% to about 45% in the potential range of sharp increase of current
905 density on the polarization curve j_{Co} vs. E in Fig. 2.25b. At potentials
906 more negative than -1.20 V, η_j is practically independent of poten-
907 tial value.
908   Comparing polarization curves (j_{tot}) recorded onto GC and Co
909 electrodes (Fig. 2.35) one can see that the electrodeposition process
910 onto Co electrode commences at more positive potentials, while the
911 current density of the second inflection point, as well as the current
912 density at potentials more negative than that point, is smaller. Such
913 behavior is reasonable to expect since the overvoltage for Co elec-
914 trodeposition should be higher for GC than for Co electrodes, while
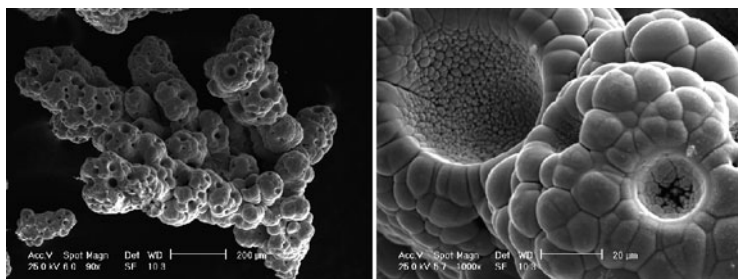915 at the same time the increase of the real surface area onto Co

Fig. 2.36 SEM micrographs of the agglomerates electrodeposited at j_{pd} marked in Fig. 2.11 for GC and Co electrode (Reprinted from [91] with the permission of Elsevier.)

electrode should be smaller than that on the GC electrode since the 916
epitaxial growth of Co onto Co electrode should be expected at the 917
beginning of the electrodeposition process. 918

The morphology of Co powder agglomerates electrodeposited at 919
j_{pd} (marked in Fig. 2.35), independently of the substrate (GC or Co), 920
is presented in Fig. 2.36. It is practically the same as that for Co 921
powder electrodeposited at $j_{pd}(2)$ from sulfate electrolyte [90], except 922
that all nodular endings possess flat surface [91] which is actually 923
composed of very thin (about 0.1 μm) and about 1 μm long crystals of 924
Co, as shown in Fig. 2.33. 925

2.5.3 Electrodeposition of Fe Powder 926

Iron powder was electrodeposited from the solution containing 927
1 M NH_4Cl + 0.2 M $Na_3C_6H_5O_7$ + 0.1 M $FeCl_2$, pH 4.0. Polariza- 928
tion curves were recorded on the glassy carbon disc by the procedure 929
explained in Sect. 2.2. The powders for SEM and XRD analyses 930
were electrodeposited at the current density j_{pd} (marked in Fig. 2.37) 931
by the procedure explained in Sect. 2.2. 932

The polarization curve for Fe powder electrodeposition is shown 933
in Fig. 2.37. The current efficiency for Fe powder electrodeposition is 934
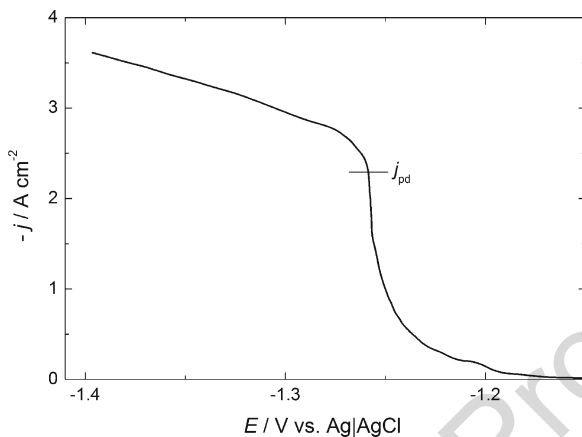very small (<2%) and the polarization curves for Fe powder 935

Fig. 2.37 Polarization curve for Fe powder electrodeposition

936 electrodeposition (j_{tot}) and for hydrogen evolution (j_H) practically
937 overlap. Accordingly, η_j vs. E is not presented [103].

938   The diffractogram of electrodeposited Fe powder is presented in
939 Fig. 2.38. The dimensions of crystallites were about 20 nm. Because
940 of very small dimensions of crystallites only phases with the highest
941 intensity were determined with high certainty, and these were peaks
942 of the α—Fe phase (▲).

943   Agglomerates of the order of 100–200 μm with big cone-shaped
944 cavities in Fig. 2.39a and small number of deep cylindrical cavities
945 Fig. 2.39b are characteristic for this powder, as shown in Fig. 2.39 [103].

946   The surface of nodular endings on the agglomerates is not as flat as
947 in the case of Co powder agglomerates, and the formation of new
948 crystals on compact surface can be detected (Fig. 2.39b).

949 ## 2.5.4   Electrodeposition of Ni Powder

950 Electrodeposition of Ni powder was investigated from three different
951 solutions: 1 M $(NH_4)_2SO_4$ + 0.7 M NH_4OH + 0.1 M $NiSO_4$—sulfate
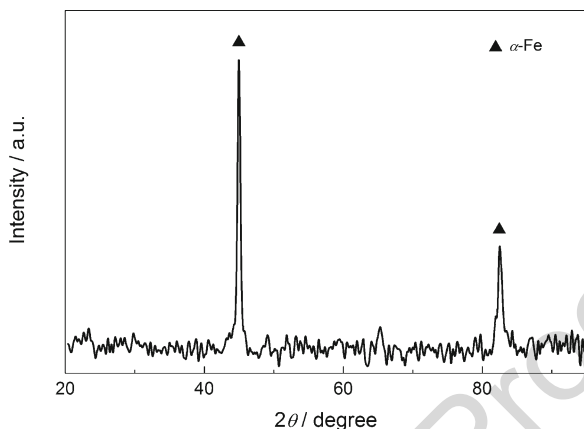952 solution; 1 M NH_4Cl + 0.7 M NH_4OH + 0.1 M $NiCl_2$—chloride

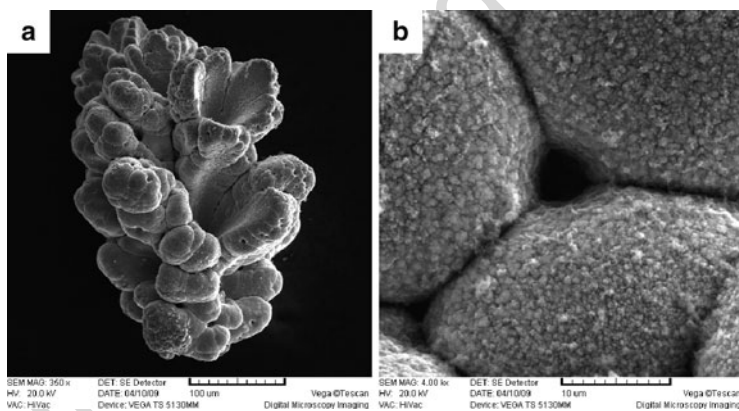**Fig. 2.38** X-ray diffraction pattern of electrodeposited Fe powder

Fig. 2.39 (**a**) SEM micrograph of the agglomerates obtained in electrodeposited Fe powder. (**b**) Deep cylindrical cavity surrounded with spherical compact surface covered with new crystals (Reprinted from [103] with the permission of Elsevier.)

solution; and 1M NH_4Cl + 0.2 M $Na_3C_6H_5O_7$ + 0.1 M $NiCl_2$—citrate solution.

The polarization curve and the corresponding current efficiency potential dependence recorded onto GC electrode from sulfate solution are shown in Fig. 2.40.

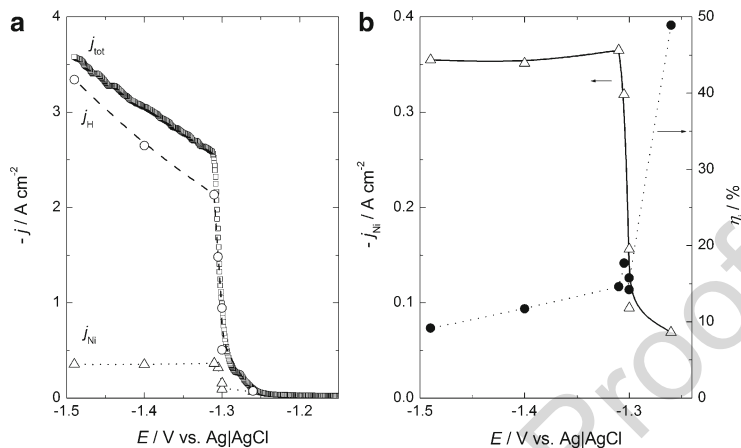**Fig. 2.40** (**a**) Polarization curve for the electrodeposition of Ni powder from sulfate solution after IR drop correction (j_{tot}), polarization curve for hydrogen evolution (j_H) and polarization curve for Ni powder electrodeposition (j_{Ni}) after subtraction of the current density for hydrogen evolution. (**b**) Polarization curve for Ni powder electrodeposition (j_{Ni}) and corresponding current efficiency curve (η_j) (Reprinted from [90] with the permission of Elsevier.)

The process of Ni electrodeposition commences at about -1.25 V with the second inflection point at -1.30 V. The curve for Ni powder electrodeposition (j_{Ni}) is characterized with well-defined current density plateau in the potential range between -1.30 V and -1.40 V. The current efficiency (η_j) is seen to decrease sharply from about 50% to about 15% in the potential range of sharp increase of current density on the polarization curve j_{Ni} vs. E in Fig. 2.40b. At potentials more negative than -1.30 V η_j slightly decreases to about 10% at -1.40 V.

The polarization curve and the corresponding current efficiency potential dependence recorded onto GC electrode from chloride solution [91] are shown in Fig. 2.41. As can be seen in Fig. 2.41a the electrodeposition of Ni in this solution commences at slightly more negative potential of about -1.28 V, while j_H is lower than that recorded in sulfate solution and accordingly the current efficiency (η_j) is higher, sharply decreasing from about 90% to about 45% in the potential range of sharp increase of current density on the
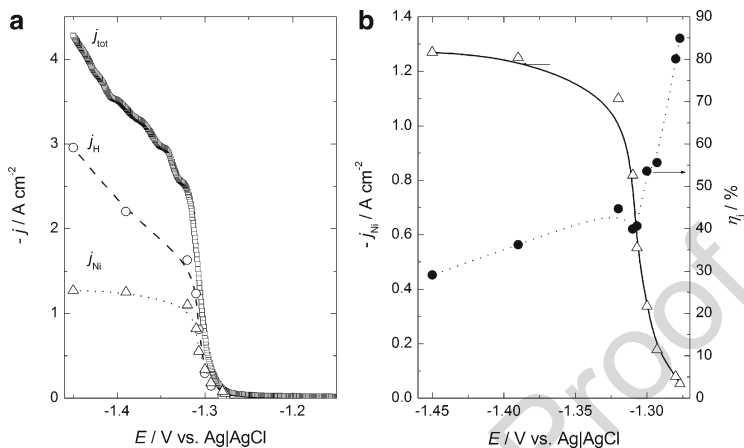
Fig. 2.41 (**a**) Polarization curve for the electrodeposition of Ni powder from chloride solution after IR drop correction (j_{tot}), polarization curve for hydrogen evolution (j_H), and polarization curve for Ni powder electrodeposition (j_{Ni}) after subtraction of the current density for hydrogen evolution. (**b**) Polarization curve for Ni powder electrodeposition (j_{Ni}) and corresponding current efficiency curve (η_j) (Reprinted from [91] with the permission of Elsevier.)

polarization curve j_{Ni} vs. E in Fig. 2.41b. At potentials more negative than -1.30 V η_j slightly decreases to about 30% at -1.40 V.

The polarization curve recorded onto GC electrode from citrate solution is compared with those from sulfate and chloride solutions in Fig. 2.42. Similar polarization curves from all solutions are obtained, except that the current density after the second inflection point for citrate solution is half of that for sulfate and chloride solutions. The (η_j) vs. E dependence recorded in citrate solution is similar to those for sulfate and chloride solutions, being practically constant (20%) in the potential range of current density plateau on the polarization curve j_{Ni} vs. E.

Samples for SEM, EDS, and XRD analyses were electrodeposited at the j_{pd} values marked in the figure, $j_{pd}(sul) = -0.5$ A cm^{-2}, $j_{pd}(chl) = -2.0$ A cm^{-2}, $j_{pd}(cit) = -1.4$ A cm^{-2}.

X-ray diffraction pattern of nickel powder sample is shown in Fig. 2.43. The same diffractograms are obtained for Ni powders electrodeposited from all three solutions. As can be seen the powder
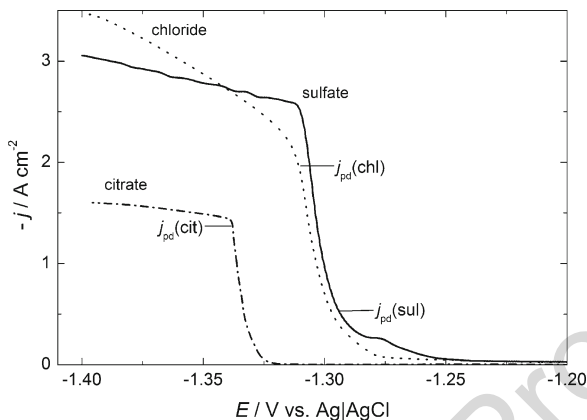
Fig. 2.42 Polarization curves for the electrodeposition of Ni powder from citrate, sulfate and chloride solutions after IR drop correction; corresponding current densities for powder electrodeposition, $j_{pd}(cit)$, $j_{pd}(sul)$, and $j_{pd}(chl)$ are marked in the figure

992 consists only of the face-centered cubic nickel phase (β-Ni) with the
993 lattice parameter of $a = 3.5231$ Å.
994   In Fig. 2.44a, b are shown SEM micrographs of Ni powder
995 electrodeposited from sulfate solution at $j_{pd}(sul) = -0.5$ A cm^{-2}.
996 As can be seen typical cauliflower-type agglomerates are obtained
997 with the size of agglomerates varying from about 5 μm to about
998 50 μm. No hydroxide or oxide impurities were detected, which is in
999 accordance with the literature data [74, 77, 83]. Ni powder
1000 agglomerates are very similar to those of copper [102] and since
1001 the mechanism of their growth has already been explained, it is not
1002 necessary to discuss the mechanism of their growth.
1003   SEM micrographs of Ni powder electrodeposited from chloride
1004 solution at $j_{pd}(chl) = -2.0$ A cm^{-2} are shown in Fig. 2.45a, b.
1005 Typical spongy-like agglomerates are obtained with the size of
1006 agglomerates varying from about 200 μm to about 600 μm. As in
1007 the case of Co powder electrodeposited at high current densities from
1008 chloride and sulfate solution, cone-shaped (Fig. 2.45a) and cylindri-
1009 cal cavities (Fig. 2.45b) are obtained on the surface of Ni agg-
1010 lomerates. No fern-like dendrites were formed on the bottom of
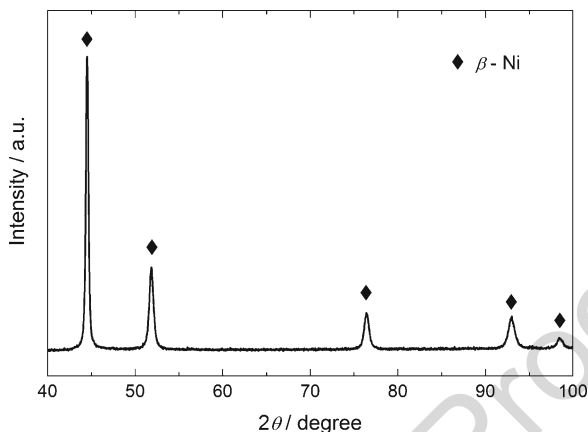1011 cylindrical cavities, indicating that the agglomerates were detached

Fig. 2.43 X-ray diffraction pattern of electrodeposited Ni powder (Reprinted from [99] with the permission of Springer-Verlag.)
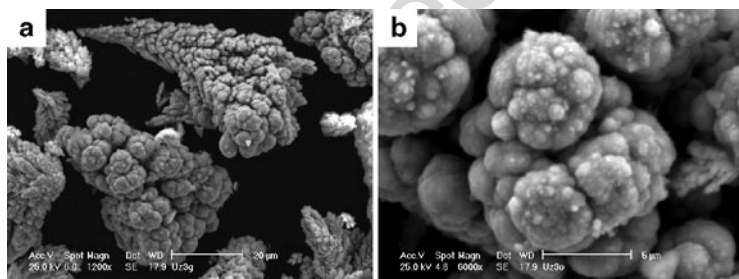

Fig. 2.44 SEM micrographs of the agglomerates electrodeposited at j_{pd}(sul) marked in Fig. 2.42 for GC electrode (Reprinted from [90] with the permission of Elsevier.)

from the electrode surface before the liberation of hydrogen bubbles formed on their surfaces, as explained in Sect. 2.5.2.2.

From the citrate solution completely different morphology of electrodeposited Ni powder is obtained [103], as shown in Fig. 2.46. Typical Ni powder is characterized by the presence of flake-like particles of the maximum size of about 50 μm covered with nodules of mainly flat surfaces. The formation of a second zone of
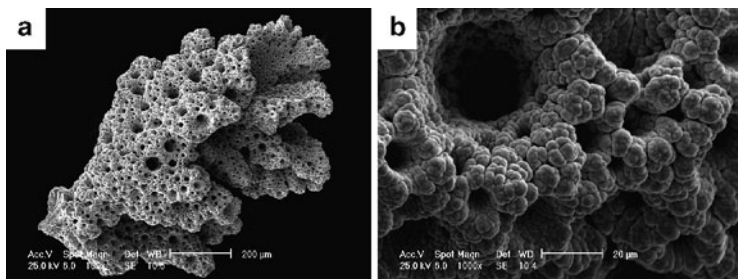
Fig. 2.45 SEM micrographs of the agglomerates electrodeposited at j_{pd}(chl) marked in Fig. 2.42 for GC electrode (Reprinted from [91] with the permission of Elsevier.)
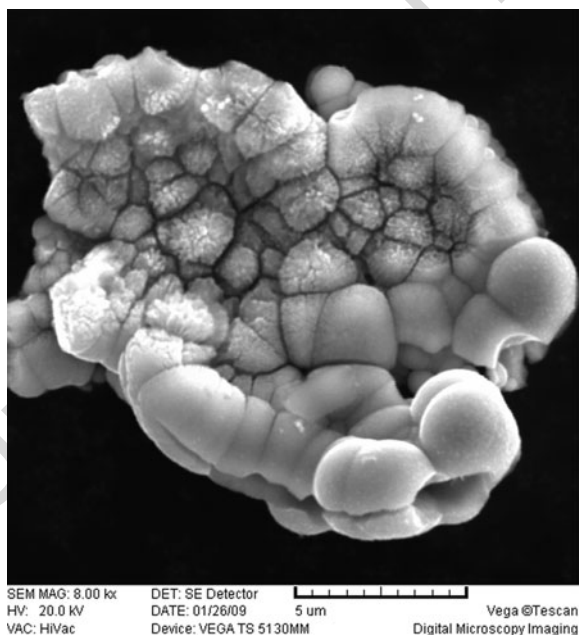

Fig. 2.46 Typical Ni powder particle electrodeposited at j_{pd}(cit) in citrate solution (Reprinted from [103] with the permission of Elsevier.)

dendrites (beginning with the formation of small crystals in the upper   1019
part of the particle presented in Fig. 2.46), typical for powder depo-   1020
sition [99], could be detected on some particles.   1021

2.6   Conclusions   1022

Powders of both academically and technologically important metals,   1023
such as silver, lead, cadmium, cobalt, nickel, and iron, were produced   1024
by the electrolytic processes. The constant regimes of electrolysis   1025
and the regime of pulsating overpotential (PO) were used for the   1026
electrochemical synthesis of powders of these metals. Morphologies   1027
of such obtained powders were characterized by the scanning   1028
electron microscopy and optical microscopy, as well as by X-ray   1029
diffraction techniques.   1030

   The processes of electrochemical deposition of silver from   1031
nitrate solutions, lead, and cadmium are characterized by high   1032
exchange current densities, and single and two-dimensional (2D)   1033
dendrites were largely formed by electrodepositions of these   1034
metals. On the other hand, very branchy dendrites constructed   1035
from corncob-like elements (similar to copper dendrites) were   1036
obtained by the electrodeposition of silver from ammonium solu-   1037
tion which is characterized by the medium exchange current   1038
density. Also, the application of the PO regime strongly affected   1039
the morphology of silver and lead powder particles and mathemati-   1040
cal model was presented to explain the change of morphology   1041
of particles in relation to the one obtained in the constant potentio-   1042
static mode.   1043

   Ni powder is characterized by cauliflower-like type particles in   1044
ammoniacal electrolytes, while in citrate electrolytes the flakes of the   1045
maximum size of about 50 μm covered with nodules of mainly flat   1046
surfaces were detected. On some particles the formation of a second   1047
zone of dendrites (beginning with the formation of small crystals)   1048
could be detected. The Fe powder particles of the size of about   1049
200 μm also contain nodules of flat surfaces, but they are   1050
characterized by the presence of cone-shaped cavities. In the case   1051
of Co powder, generally two types of particles were detected   1052

(1) dendrite particles and (2) different types of agglomerates being characterized by the presence of cavities and fern-like dendrites formed on the bottom of most of them. These agglomerates can further be divided into three groups (a) compact agglomerates; (b) spongy-like agglomerates of different shapes, and (c) balls of the size of about 200 μm with more or less dense cauliflower structure on their surface. The growth mechanism of all agglomerates detected in the electrodeposited Co powder has been explained. The type of the agglomerate depends on its growth stage, i.e., on the moment when it becomes detached from the electrode surface.

References

1. Pavlović MG, Popov KI (2005) Electrochem Encycl. http://electrochem.cwru.edu/ed/encycl/
2. Winand R (1998) Electrochim Acta 43:2925
3. Price PB, Vermilyea DA (1958) J Chem Phys 28:720
4. Djokić SS, Nikolić ND, Živković PM, Popov KI, Djokić NS (2011) ECS Trans 33:7
5. Popov KI, Krstajić NV, Popov SR (1984) Surf Technol 22:245
6. Popov KI, Djokić SS, Grgur BN (2002) Fundamental aspects of electrometallurgy. Kluwer Academic/Plenum, New York
7. Nikolić ND, Popov KI, Pavlović LjJ, Pavlović MG (2006) J Electroanal Chem 588:88
8. Nikolić ND, Popov KI, Pavlović LjJ, Pavlović MG (2006) Surf Coat Technol 201:560
9. Nikolić ND, Popov KI, Pavlović LjJ, Pavlović MG (2007) Sensors 7:1
10. Nikolić ND, Branković G, Pavlović MG, Popov KI (2008) J Electroanal Chem 621:13

11. Nikolić ND, Popov KI (2010) Hydrogen co-deposition effects on the structure of electrodeposited copper. In: Djokić SS (ed) Electrodeposition: theory and practice, vol 48, Modern aspects of electrochemistry. Springer, New York, pp 1–70

12. Nikolić ND, Pavlović LjJ, Pavlović MG, Popov KI (2007) Electrochim Acta 52:8096

13. Nikolić ND, Pavlović LjJ, Branković G, Pavlović MG, Popov KI (2008) J Serb Chem Soc 73:753

14. Nikolić ND, Pavlović LjJ, Pavlović MG, Popov KI (2008) Powder Technol 185:195

15. Nikolić ND, Branković G, Pavlović MG, Popov KI (2009) Electrochem Commun 11:421

16. Nikolić ND, Branković G, Maksimović VM, Pavlović MG, Popov KI (2010) J Solid State Electrochem 14:331

17. Nikolić ND, Branković G, Maksimović VM, Pavlović MG, Popov KI (2009) J Electroanal Chem 635:111

18. Nikolić ND, Branković G, Popov KI (2011) Mater Chem Phys 125:587

19. Nikolić ND, Branković G (2010) Electrochem Commun 12:740

20. Nikolić ND, Branković G, Maksimović V. J Solid State Electrochem. doi: 10.1007/s10008-011-1331-x

21. Popov KI, Vojnović M, Rikovski G (1968) Hemijska Industrija 8:1392 (in Serbian)

22. Trasatti S (1972) J Electroanal Chem 39:163

23. Popov KI, Pavlović MG, Stojilković ER, Radmilović V (1996) J Serb Chem Soc 61:47

24. Pavlović MG, Maksimović MD, Popov KI, Kršul MB (1978) J Appl Electrochem 8:61

25. Barton JL, Bockris JO'M (1962) Proc R Soc A A268:485

26. Bek RYu, Kudryavtsev NT (1961) Zh Prikl Khim 34:2013

27. Bek RYu, Kudryavtsev NT (1961) Zh Prikl Khim 34:2020

28. Arouete S, Blurton KF, Oswin HG (1969) J Electrochem Soc 116:166

29. Popov KI, Keča DN, Anđelić MD (1978) J Appl Electrochem 8:19

30. Popov KI, Anđelić MD, Keča DN (1978) Glasnik Hem Društva Beograd 43:67

31. Popov KI, Pavlović MG, Remović GŽ (1991) J Appl Electrochem 21:743

32. Popov KI, Maksimović MD, Zečević SK, Stojić MR (1986) Surf Coat Technol 27:117

33. Despić AR, Popov KI (1972) Transport controlled deposition and dissolution of metals. In: Conway BE, Bockris JO'M (eds) Modern aspects of electrochemistry, vol 7. Plenum, New York, pp 199–313

34. Popov KI, Maksimović MD (1989) Theory of the effect of electrodeposition at periodically changing rate on the morphology of metal deposition. In: Conway BE, Bockris JO'M, White RE (eds) Modern aspects of electrochemistry, vol 19. Plenum press, New York, pp 193–250

35. Popov KI, Pavlović MG, Jovićević JN (1989) Hydrometallurgy 23:127

1135 36. Romanov VV (1963) Zh Prikl Khim 36:1050
1136 37. Romanov VV (1961) Zh Prikl Khim 34:2692
1137 38. Romanov VV (1963) Zh Prikl Khim 36:1057
1138 39. Popov KI, Maksimović MD, Simičić NV, Krstajić NV (1984) Surf Technol
1139   22:159
1140 40. Vijh AK, Randin JP (1977) Surf Technol 5:257
1141 41. Nikolić ND, Lačnjevac U, Branković G, to be published   AU5
1142 42. Popov KI, Živković PM, Krstić SB, Nikolić ND (2009) Electrochim Acta
1143   54:2924
1144 43. Popov KI, Živković PM, Nikolić ND (2010) The effect of morphology of
1145   activated electrodes on their electrochemical activity. In: Djokić SS (ed)
1146   Electrodeposition: theory and practice, vol 48, Modern aspects of electro-
1147   chemistry. Springer, New York, pp 163–213
1148 44. Bockris JO'M, Reddy AKN, Gamboa-Aldeco M (2000) Modern electrochem-
1149   istry: fundamentals of electrodics, vol 2A, 2nd edn. Kluwer Academic/Plenum,
1150   New York, p 1107
1151 45. Wranglen G (1960) Electrochim Acta 2:130
1152 46. Diggle JW, Despić AR, Bockris JO'M (1969) J Electrochem Soc 116:1503
1153 47. Popov KI, Krstajić NV, Čekerevac MI (1996) The mechanism of formation
1154   of coarse and disperse electrodeposits. In: White RE, Conway BE, Bockris
1155   JO'M (eds) Modern aspects of electrochemistry, vol 30. Plenum, New York,
1156   pp 261–312
1157 48. Popov KI, Stojilković ER, Radmilović V, Pavlović MG (1997) Powder
1158   Technol 93:55
1159 49. Popov KI, Maksimović MD, Trnjančev JD, Pavlović MG (1981) J Appl
1160   Electrochem 11:239
1161 50. Popov KI, Pavlović MG, Maksimović MD (1982) J Appl Electrochem
1162   12:525
1163 51. Pangarov NA (1964) Electrochim Acta 9:21
1164 52. Pangarov NA, Vitkova SD (1966) Electrochim Acta 11:1733
1165 53. Popov KI, Čekerevac MI (1989) Surf Coat Technol 37:435
1166 54. Čekerevac MI, Popov KI (1989) Surf Coat Technol 37:441
1167 55. Calusaru A (1979) Electrodeposition of powders from solutions. Elsevier,
1168   New York, pp 363–389
1169 56. Mathers, Turner (1932) British Patent No. 403281
1170 57. Mathers (1932) Met Ind (NY) 30:321, 396, 368
1171 58. Huppomann WJ, Dalal K (1986) Metallographic atlas of powder metallurgy.
1172   Werlag Schmid GmbH, pp 21–63
1173 59. Kudryavtsev N, Petrova A (1932) Novosti tehniki, N.K.T.R 171
1174 60. Hardy C, Mantell C (1937) French Patent No. 814500
1175 61. Hardy C, Mantell C (1938) US Patent No. 2157699
1176 62. Kudryavtsev N, Tereshkocitch E (1948) Zhur Prikl Khim 12:1298
1177 63. Borok B, Olhov I (1948) Metallurgy of powders, pp 34–35
1178 64. Kalaida T, Rozenzweig S (1936) Collect Works Chem Cells 1:48
1179 65. Balshin M (1935) NIIMASH 12:5

66. Mantell C (1939) British Patent No. 503306   1180
67. Casey H (1949) US Patent No. 2481079   1181
68. Wranglen G (1950) Acta Polytechnica Electr Eng Ser 2:69   1182
69. Sanvordenkar K, Tendolkar G (1954) J Indian Chem Soc Ind News Ed 17:13   1183
70. Rozenzweig S (1936) Sov avt 46284   1184
71. Gardam G (1951) Powder Metall 6:75; (1947) Spec Rep 38:3   1185
72. Zhelibo EP, Aryupina KA, Natanson EM (1973) Powder Metall 122:14   1186
73. Chu CM, Wan CC (1992) J Mater Sci 27:6700   1187
74. Fedorova O (1938) Zh Obsch Khim 8:1711   1188
75. Hardy C, Mantell C (1937) French Patent No. 815500   1189
76. Loshkarev M, Gernostaleva O, Kriukova A (1946) Zhur Prikl Khim 19:739   1190
77. Levin A (1946) Zhur Prikl Khim 19:779   1191
78. Hiruma K (1949) J Electrochem Soc Jpn 17:160   1192
79. Drozdov B (1955) Zhur Prikl Khim 1:45   1193
80. Nicol A (1946) CR 222:1043   1194
81. Wranglen G (1950) Acta Polytechnica Electr Eng Ser 2:69   1195
82. Kuroda M, Yto G, Shimizu Y (1953) Rep Sci Res (Japan) 29:429   1196
83. Mantell C (1941) US Patent No. 2233103   1197
84. Pavlović MG, Hadžismajlović DŽ, Popov KI (1991) Chem Ind 45:39   1198
85. Santos JS, Matos R, Trivinho-Strixino F, Pereira EC (2007) Electrochim   1199
    Acta 53:644   1200
86. Gabe DR (1997) J Appl Electrochem 27:908   1201
87. Palomar-Pardave M, Scharifker BR, Arce EM, Romero-Romo M (2005)   1202
    Electrochim Acta 50:4736   1203
88. Rojas M, Fan CL, Miao HJ, Piron DL (1992) J Appl Electrochem 22:1135   1204
89. Dıaz SL, Calderon JA, Barcia OE, Mattos OR (2008) Electrochim Acta   1205
    53:7426   1206
90. Jović VD, Jović BM, Pavlović MG (2006) Electrochim Acta 51:5468   1207
91. Jović VD, Jović BM, Maksimović V, Pavlović MG (2007) Electrochim Acta   1208
    52:4254   1209
92. Vogt H, Balzer RJ (2005) Electrochim Acta 50:2073   1210
93. Vogt H (1997) Electrochim Acta 42:2695   1211
94. Vogt H (1999) J Appl Electrochem 29:137   1212
95. Wüthrich R, Fascio V, Bleuler H (2004) Electrochim Acta 49:4005   1213
96. Wüthrich R, Bleuler H (2004) Electrochim Acta 49:1547   1214
97. Wüthrich R, Commninellis Ch, Bleuler H (2005) Electrochim Acta 50:5242   1215
98. Lowenheim FA (1974) Modern electroplating, 3rd edn. Wiley-Interscience,   1216
    New York   1217
99. Jović VD, Maksimović V, Pavlović MG, Popov KI (2006) J Solid State   1218
    Electrochem 10:373   1219
100. Popov KI, Krstić SB, Obradović MC, Pavlović MG, Pavlović LjJ, Ivanović   1220
    ER (2004) J Serb Chem Soc 69:43   1221
101. Murashova IB, Pomosov AV (1989) Itogi nauki i tekhniki, Seria   1222
    Elektrokhimiya, vol 30. VINITI, Moskva, p 90   1223
102. Popov KI, Krstajić NV (1983) J Appl Electrochem 13:775   1224
103. Lačnjevac U, Jović BM, Jović VD (2009) Electrochim Acta 55:535   1225